Mon. Not. R. Astron. Soc. **368,** 48–64 (2006) doi:10.1111/j.1365-2966.2006.10099.x

Multifrequency observations of the jets in the radio galaxy NGC 315

R. A. Laing,[1⋆] J. R. Canvin,[2,3] W. D. Cotton[4] and A. H. Bridle[4]

[1]*European Southern Observatory, Karl-Schwarzschild-Straße 2, D-85748 Garching-bei-München, Germany*
[2]*School of Physics, University of Sydney, A28, Sydney, NSW 2006, Australia*
[3]*University of Oxford, Department of Astrophysics, Denys Wilkinson Building, Keble Road, Oxford OX1 3RH*
[4]*National Radio Astronomy Observatory, 520 Edgemont Road, Charlottesville, VA 22903-2475, USA*

Accepted 2006 January 19. Received 2006 January 19; in original form 2005 November 22

ABSTRACT

We present images of the jets in the nearby radio galaxy NGC 315 made with the Very Large Array at five frequencies between 1.365 and 5 GHz with resolutions between 1.5 and 45 arcsec. Within 15 arcsec of the nucleus, the spectral index of the jets is $\alpha = 0.61$. Further from the nucleus, the spectrum is flatter, with significant transverse structure. Between 15 and 70 arcsec from the nucleus, the spectral index varies from ≈0.55 on-axis to ≈0.44 at the edge. This spectral structure suggests a change of dominant particle acceleration mechanism with distance from the nucleus and the transverse gradient may be associated with shear in the jet velocity field. Further from the nucleus, the spectral index has a constant value of 0.47. We derive the distribution of Faraday rotation over the inner ±400 arcsec of the radio source and show that it has three components: a constant term, a linear gradient (both probably due to our Galaxy) and residual fluctuations at the level of 1–2 rad m^{-2}. These residual fluctuations are smaller in the brighter (approaching) jet, consistent with the idea that they are produced by magnetic fields in a halo of hot plasma that surrounds the radio source. We model this halo, deriving a core radius of ≈225 arcsec and constraining its central density and magnetic field strength. We also image the apparent magnetic field structure over the first ±200 arcsec from the nucleus.

Key words: magnetic fields – MHD – polarization – galaxies: individual: NGC 315 – galaxies: jets – radio continuum: galaxies.

1 INTRODUCTION

The giant FRI (Fanaroff & Riley 1974) radio source NGC 315 was first imaged by Bridle et al. (1976), who showed that it has an angular size of nearly 1°. The extended radio structure is described in more detail by Bridle et al. (1979), Fomalont et al. (1980), Willis et al. (1981), Jägers (1987), Venturi et al. (1993), Mack et al. (1997) and Mack et al. (1998). The main jet has also been imaged extensively on parsec scales (Linfield 1981; Venturi et al. 1993; Cotton et al. 1999; Xu et al. 2000). X-ray emission from the first 10 arcsec of the main jet was detected by Worrall, Birkinshaw & Hardcastle (2003), but no optical emission from this region has yet been reported.

The source is associated with a giant elliptical galaxy at a redshift of 0.01648 (Trager et al. 2000), giving a scale of 0.335 kpc arcsec^{-1} for our adopted cosmology (Hubble constant $H_0 = 70\,\mathrm{km\,s^{-1}\,Mpc^{-1}}$, $\Omega_\Lambda = 0.7$ and $\Omega_\mathrm{M} = 0.3$). NGC 315 is a member of a group or poor cluster of galaxies (Nolthenius 1993; Miller et al. 2002) located in one of the filaments of the Pisces–Perseus supercluster (Huchra et al. 1990; Enßlin et al. 2001). *Hubble Space Telescope* images (Verdoes Kleijn et al. 1999) show a 2.5-arcsec diameter dust lane and a nuclear point source. The dust lane is associated with a disc of ionized gas which is probably in ordered rotation (Noel-Storr et al. 2003). CO emission, also with a line profile indicating rotation, was detected by Leon et al. (2003). The inferred mass of molecular hydrogen is $(3.0 \pm 0.3) \times 10^8\,\mathrm{M_\odot}$ and the cold gas is likely to be cospatial with the dust. H I absorption against the nucleus was detected by van Gorkom et al. (1989). There is evidence for a weak, polarized broad Hα line in the nuclear spectrum (Ho et al. 1997; Barth, Filippenko & Moran 1999; Noel-Storr et al. 2003). Hot gas associated with the galaxy has been imaged using *ROSAT* and *Chandra* (Worrall & Birkinshaw 2000; Worrall et al. 2003).

Within ≈90 arcsec of the nucleus, the jets in NGC 315 are initially narrow, then expand rapidly ('flare') and recollimate (Bridle 1982; Canvin et al. 2005). We have modelled the inner ±70 arcsec of this *flaring region* as a two-sided, symmetrical, relativistic flow, fitting to deep, high-resolution Very Large Array (VLA) observations at 5 GHz in order to derive the three-dimensional distributions of velocity, proper emissivity and magnetic field structure (Canvin et al. 2005). Our main conclusions are as follows.

⋆E-mail: rlaing@eso.org

(i) The jets are inclined by $38^\circ \pm 2^\circ$ to the line of sight.

(ii) Where they first brighten, their on-axis velocity is $\beta = v/c \approx 0.9$. They decelerate to $\beta \approx 0.4$ between 8 and 18 kpc from the nucleus (15–33 arcsec in projection) and the velocity thereafter remains constant.

(iii) The ratio of the speed at the edge of the jet to its value on-axis ranges from ≈0.8 close to the nucleus to ≈0.6 further out.

(iv) The longitudinal profile of proper emissivity is split into three power-law regions separated by shorter transition zones and the emission is intrinsically centre-brightened.

(v) To a first approximation, the magnetic field evolves from a mixture of longitudinal and toroidal components to predominantly toroidal by 26 kpc (48 arcsec in projection).

(vi) Simple adiabatic models fail to fit the emissivity variations.

In the present paper, we investigate the energy spectrum of the relativistic particles in the jets of NGC 315 in the context of the models developed by Canvin et al. (2005). We use VLA observations at frequencies between 1.365 and 5 GHz[1] to derive the spectrum of the jets at resolutions of 5.5 and 1.5 arcsec and relate the observed spectral gradients to velocity, emissivity and field structure. A separate paper (Worrall et al., in preparation) will describe the radio structure of the main jet at high resolution and its relation to new *Chandra* images.

We also determine the variations of Faraday rotation over the jets and test the hypothesis that these result from magnetic field irregularities in hot, X-ray emitting plasma associated with the surrounding group of galaxies. Finally, we determine the apparent magnetic field structure of the jets on scales larger than those covered by Canvin et al. (2005).

In Section 2, we describe the observations and their reduction. The total-intensity images are presented in Section 3 and we use them to derive distributions of spectral index in Section 4. We then discuss the distributions of Faraday rotation (Section 5) and apparent magnetic field structure (Section 6) derived from observations of linear polarization. Section 7 summarizes our main results.

2 OBSERVATIONS AND IMAGES

2.1 Observations

VLA data were obtained at 4.985 GHz in the B, C/D and A/D configurations as described by Venturi et al. (1993) and Cotton et al. (1999). These were supplemented by additional observations in the A and C configurations with a centre frequency of 4.860 GHz to give complete coverage of the spatial scales accessible to the VLA in a single pointing. In order to map Faraday rotation, we observed at 1.365, 1.413, 1.485 and 1.665 GHz in the B and C configurations of the VLA using a lower bandwidth. We also extracted observations in A configuration at 1.413 GHz from the VLA archive.[2] A journal of observations is given in Table 1.

2.2 Data reduction

All of the data reduction was done in the AIPS package. Initial amplitude and phase calibration were applied using standard methods and the flux-density scales were set using observations of 3C 48 or 3C 286. Standard instrumental polarization calibration was applied and the zero-points of ***E***-vector position angle were determined using observations of 3C 138 or 3C 286. The data for each configuration were first adjusted to a common phase centre in J2000 coordinates, imaged and self-calibrated separately. They were then concatenated in turn, starting with the widest configuration. The slight difference in centre frequency between the data sets at 4.86 and 4.985 GHz was ignored (we show in Section 5.1 that this has a negligible effect on the analysis of polarization) and we will refer to the combination as the '5 GHz data set'. At this frequency, the core showed significant variability between observations (cf. Lazio et al. 2001) and the flux density of the unresolved component in the larger-configuration data set was adjusted to match that observed with the smaller configuration when both were imaged at matched resolution. No core variability was detected at lower frequencies. A further iteration of phase self-calibration was done after each combination. Our final data sets are listed in Table 2, together with the minimum and maximum spatial scales they sample.

Our observations were designed to give the maximum sensitivity for the inner jets of NGC 315 and were therefore taken with the pointing centre on or near the nucleus. As can be seen from Table 2, the maximum spatial scale sampled adequately at 5 GHz is ≈300 arcsec. Even at *L* band, the lobe associated with the counter jet (Mack et al. 1997 and Fig. 1a) is severely attenuated by the primary-beam response of the VLA and is not visible on our images. We did not recover the total flux density of the source at any frequency, so we estimated appropriate zero-spacing flux densities

Table 1. Record of VLA observations. ν and $\Delta\nu$ are the centre frequency and bandwidth, respectively, and t is the on-source integration time.

Configuration	Date	ν (MHz)	$\Delta\nu$ (MHz)	t (min)
B	1989 April 13	4985.1	50	279
B	1995 October 25	4985.1	50	396
C/D	1996 May 10	4985.1	50	417
A/D	1996 October 07	4985.1	50	428
A	1996 November 2	4860.1	100	586
C	1997 July 12	4860.1	100	283
A	1980 December 21	1413.0	25	473
B	2001 March 19	1365.0	12.5	108
B	2001 March 19	1413.0	12.5	108
B	2001 March 19	1485.0	12.5	109
B	2001 March 19	1665.0	12.5	107
C	2001 July 17	1365.0	12.5	61
C	2001 July 17	1413.0	12.5	61
C	2001 July 17	1485.0	12.5	65
C	2001 July 17	1665.0	12.5	57

Table 2. Final *uv* data sets. The columns are: (1) centre frequency, (2) array configurations used, (3) minimum and (4) maximum spatial scales.

ν (MHz)	Configurations	Scales (arcsec) Min	Max
1365	BC	4	900
1413	ABC	1.2	900
1485	BC	4	900
1665	BC	4	900
4985/4860	ABCD	0.4	300

[1] The 5-GHz observations are those discussed by Canvin et al. (2005).

[2] In addition, we re-analysed the C-configuration data set at 8.4 GHz from Venturi et al. (1993), but poor weather during the observations precluded accurate absolute flux and polarization calibration, so we do not discuss them here.

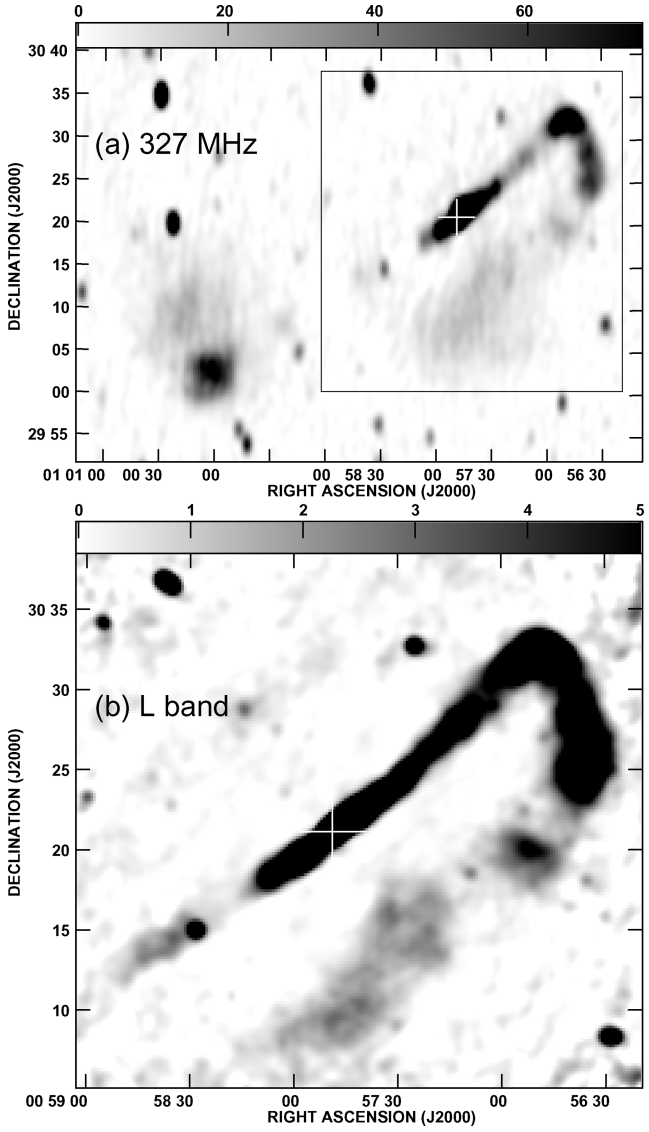

Figure 1. Grey-scales of total intensity at low resolution. (a) WSRT image at 327 MHz, showing the full extent of the radio emission from NGC 315 (Mack et al. 1997). The restoring beam is 110×55 arcsec^2 FWHM in position angle 0 and the grey-scale range is 0–75 mJy (beam area)$^{-1}$. The box marks the area covered by panel (b) and Fig. 2. (b) The mean of all four VLA *L*-band images, tapered to a resolution of 45 arcsec FWHM and corrected for attenuation by the primary beam before averaging. The grey-scale range, 0–5 mJy (beam area)$^{-1}$, has been chosen to emphasize the diffuse emission. In both panels, the cross marks the position of the core.

from the shortest-spacing visibility amplitudes. We made images at five resolutions: 45, 5.5, 2.35, 1.5 and 0.4 arcsec FWHM (full width at half-maximum), using similar baseline ranges at all frequencies and weighting the data in the *uv* plane as required. After imaging, we made both CLEAN and maximum-entropy deconvolutions. Although the latter algorithm gave slightly smoother images, it introduced a significant large-scale ripple parallel to the jet axis, whereas CLEAN gave a flat background. We therefore show the CLEAN images, although we quote quantitative results only where the two deconvolution methods agree. We also compared the *I* images made with and without zero-spacing flux densities and before and after subtraction of a local zero-level. None of these differences led to significant changes in spectral index or degree of polarization compared with the errors quoted below. After deconvolution, all of the images were corrected for primary beam attenuation. We then took averages of the *I* images at 1.365–1.665 MHz ('mean *L*-band images').

Table 3. Image resolutions and noise levels. σ_I is the off-source noise level on the *I* image; σ_P the average of the noise levels for *Q* and *U*. The noise levels were evaluated before correction for the primary beam response and apply only at the centre of the field for corrected images. Asterisks denote the images used by Canvin et al. (2005).

ν (GHz)	FWHM (arcsec)	rms noise level [μJy (beam area)$^{-1}$]	
		σ_I	σ_P
Mean *L*	45	200	–
1.365	5.5	41	35
1.413	5.5	38	34
1.485	5.5	37	33
1.665	5.5	37	30
Mean *L*	5.5	17	–
5	5.5	15	12
5*	2.35	10	8
1.413	1.5	36	36
5	1.5	10	10
5*	0.40	13	7

Data in Stokes *Q* and *U* were imaged without zero-spacing flux densities and CLEANed. A first-order correction for Ricean bias (Wardle & Kronberg 1974) was applied to the images of polarized intensity $P = (Q^2 + U^2)^{1/2}$ used to derive the degree of polarization $p = P/I$.

The off-source noise levels at the centre of the field for the final images are given in Table 3 [the 0.4-arcsec image at 5 GHz is discussed in detail by Worrall et al. (in preparation), and is therefore not considered further here]. Note that the wide-field *L*-band images at a resolution of 5.5 arcsec are significantly affected by bandwidth smearing in their outer regions, images of point sources being broadened by a factor of 2 in the radial direction at a distance of 22 arcmin from the phase centre (Taylor, Ulvestad & Perley 2004). This limitation needs to be taken into account only in the discussion of the source morphology on large scales (Section 3). Measurements of spectra are restricted to the inner 200 arcsec of the field, where the effects of bandwidth smearing are <3 per cent in peak intensity or image size for any of our frequency/resolution combinations. Our estimates of Faraday rotation, which extend to larger scales, should not be affected systematically by bandwidth smearing.

3 TOTAL INTENSITY

A grey-scale of the large-scale radio structure of NGC 315 at 327 MHz (Mack et al. 1997) is given in Fig. 1(a). Our observations are sensitive only to emission from the region indicated by the box in this figure and our mean *L*-band image of this region at a resolution of 45 arcsec FWHM is displayed in Fig. 1(b). A higher-resolution (5.5 arcsec FWHM) image of the same area is shown in Fig. 2 and a detail of the sharp bend in the main jet ≈20 arcmin from the nucleus is plotted at the same resolution but on a larger scale in Fig. 3. Finally, the 5-GHz emission from the inner 4 arcmin of the jets is shown in Fig. 4 at a resolution of 2.35 arcsec FWHM.

We refer to the NW and SE jets as the *main* and *counter* jets, as the former is brighter at most distances from the nucleus. A striking

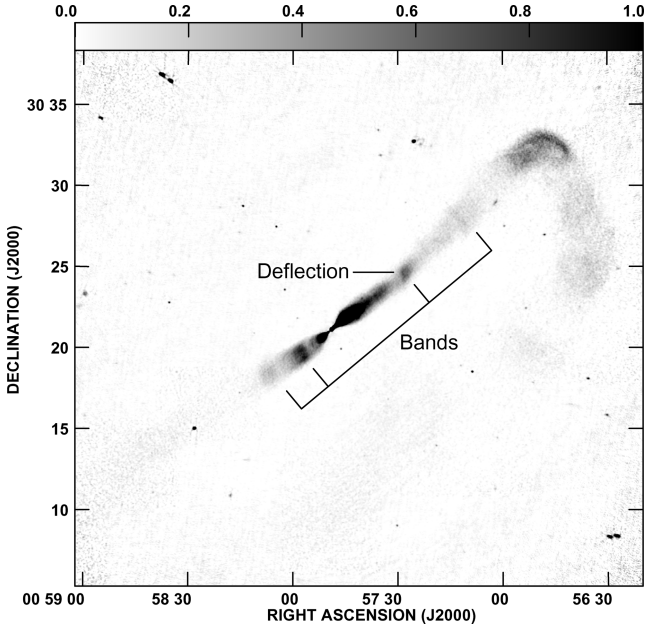

Figure 2. Grey-scale of total intensity from the mean of all four *L*-band images, corrected for attenuation by the primary beam before averaging. The resolution is 5.5 arcsec FWHM and the grey-scale range, 0–1 mJy (beam area)$^{-1}$, is marked by the labelled wedge. The area is the same as in Fig. 1(b). Note that the effects of bandwidth smearing are significant in this image (see Section 2.2).

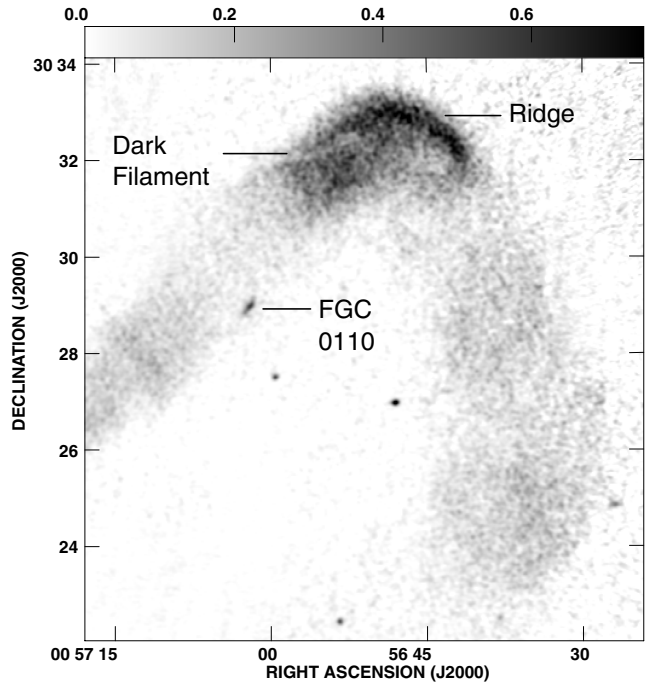

Figure 3. Grey-scale of total intensity from the mean of all four *L*-band images, corrected for attenuation by the primary beam before averaging and covering the area around the sharp bend in the main jet. The resolution is 5.5 arcsec FWHM and the grey-scale range is 0–0.75 mJy (beam area)$^{-1}$.

feature of the main jet is its almost constant width between ≈100 and 400 arcsec from the nucleus (Fig. 2). This is the *collimation shoulder* identified by Willis et al. (1981); a similar feature is visible in the counter jet, but cannot be traced out as far. The lack of

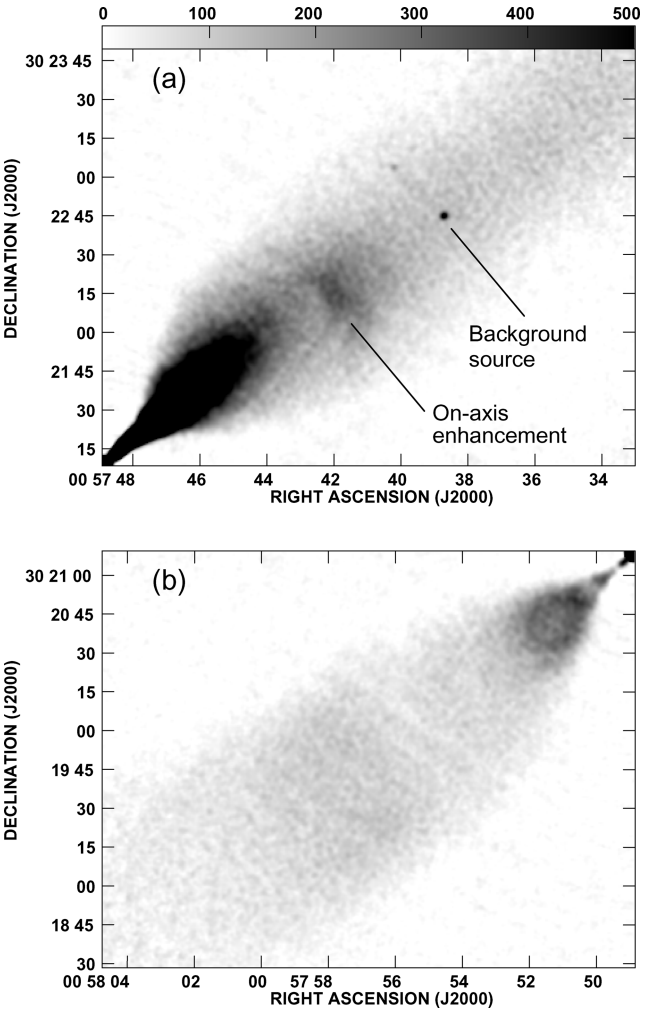

Figure 4. Grey-scale of total intensity at 5 GHz corrected for attenuation by the primary beam. The resolution is 2.35 arcsec FWHM and the grey-scale range is 0–500 μJy (beam area)$^{-1}$ as indicated by the labelled wedge. (a) Main jet, (b) counter jet.

expansion over such an extended region is surprising if the jets are confined solely by thermal plasma associated with the surrounding galaxy group, as a significant pressure gradient would be expected on scales of a few hundred arcsec (we argue in Section 5.3 that the core radius of the group-scale plasma is ≈225 arcsec). An alternative possibility is that the jets also respond to the $\boldsymbol{J} \times \boldsymbol{B}$ forces of their own toroidal fields on scales $\gtrsim$100 arcsec. In Section 6, we show that the observed polarization structure is consistent with a dominant toroidal component (see also Canvin et al. 2005), but we cannot tell from the high-frequency synchrotron emission alone whether this component is vector-ordered or has many reversals (evidence from Faraday rotation is also inconclusive; see Section 5.3). The possibility that both pressure confinement and magnetic confinement could act together to produce a collimation shoulder was discussed by Bridle, Chan & Henriksen (1981), but they assumed rather different physical parameters from those we now consider appropriate for NGC 315. Our observations show that the collimation shoulder in the main jet ends at a bright feature with a sharp edge on the side towards the nucleus, inclined by ≈60° to the jet axis. At this point (marked 'Deflection' in Fig. 2), the flow changes direction by ≈8° and re-expands with an opening angle ≈10° (defined in terms

of the jet FWHM and the angular distance from the nucleus; Willis et al. 1981). At a similar distance, the counter jet does not deflect significantly, its surface brightness decreases monotonically away from the nucleus and it expands less rapidly than the main jet (Willis et al. 1981, Fig. 1b).

The brightness distributions in both jets show large-scale 'banding' – repeated, but irregular alternation of bright and faint regions with surface brightnesses differing by factors of 1.5–2 – along their lengths on arcminute scales (Fig. 2). The brightness bands extend across both jets but their variations are slower than those in the flaring region or at the edges of the jets. These variations could, in principle, result either from periods of enhanced activity in the nucleus or from interactions between the jets and their surroundings. If they were due to fluctuations in activity in the nucleus that propagated outwards at constant velocity βc, then they would appear at projected distances $D_{\rm j}$ and $D_{\rm cj}$ in the main and counter jets, respectively, where $D_{\rm j}/D_{\rm cj} = (1+\beta\cos\theta)/(1-\beta\cos\theta)$ and $\theta \approx 38^\circ$ (Canvin et al. 2005). Any transverse velocity gradients or deceleration will complicate this expression and the former effect should distort the bands into arcs that are concave towards the nucleus. We see no obvious relation between the distances of the bands in the two jets for any plausible value of β and no evidence for systematic concave curvature of the bands beyond the flaring region. Furthermore, the most prominent banding appears to be associated with regions where the jets deflect or change their collimation properties. It therefore seems more likely that the banding is associated with ongoing interactions between the jets and their surroundings, although we cannot rule out a contribution to large-scale brightness fluctuations from slow variations in the jet output.

The remarkable 180° bend in the main jet at the West end of the source is well known from earlier observations. Our data (Fig. 1b) show the emission after the bend at a resolution comparable to the 610-MHz WSRT image presented by Mack et al. (1997). The brightness distribution at the first part of the bend (where the jet deflects by $\approx 100^\circ$) shows complex structure at 5.5-arcsec resolution. A bright ridge runs along the outside edge, with a lane of reduced emission next to it (both features are labelled on Fig. 3). Note that the suggestion that the flow is re-energized by an intergalactic shock (Enßlin et al. 2001) applies to emission further downstream, after the second bend. The compact knot of emission at the SW edge of the jet just before the bend (Fig. 3) coincides in location and shape with the optical emission from the flattened background galaxy FGC 0110 ($z = 0.021965$) and appears not to be physically related to NGC 315.

The source at right ascension $00^{\rm h}\,57^{\rm m}\,38\overset{\rm s}{.}710$, declination $30^\circ\,22'\,44\overset{''}{.}99$ (J2000; labelled 'Background source' in Fig. 4a) is unresolved and has a flat spectrum. The polarized flux density and ***E***-vector position angle vary smoothly across this position, consistent with addition of an unpolarized point source to the jet emission. There is a faint optical counterpart on the Digital Sky Survey and an X-ray point source is detected at a consistent position with the *ROSAT* PSPC (Worrall & Birkinshaw 2000; Fig. 2). The source is likely to be a background quasar, despite its location on the projected jet axis. There is a strong, diffuse component of emission on the axis of the main jet ('On-axis enhancement' in Fig. 4a) at ≈225 arcsec from the nucleus, with no obvious counterpart in the counter jet.

The 2.35-arcsec resolution images illustrate the initial flaring of the jets (discussed in detail by Canvin et al. 2005 and Worrall et al., in preparation) followed by recollimation to an almost uniform diameter (Willis et al. 1981; Bridle 1982). Although similar behaviour is observed in other sources (Laing & Bridle 2002a; Canvin & Laing 2004), the physical scale on which NGC 315 flares and recollimates is unusually large. This is probably a consequence of the low external density (Worrall et al. 2003), and we will explore this idea quantitatively elsewhere, using the conservation-law approach developed by Laing & Bridle (2002b). The jets in NGC 315 bend slightly as they recollimate, from a position angle of $-48\overset{\circ}{.}5$ close to the nucleus to $-52\overset{\circ}{.}8$ at distances $\gtrsim$100 arcsec from the nucleus. The outer isophotes of the main and counter jets are very similar before the bend, but the counter jet is slightly wider at larger distances. The main jet is brighter than the counter jet *on-axis* at all distances from the nucleus, but the counter jet is brighter at the *edge* between ≈100 and 200 arcsec. In the flaring region, by contrast, the main jet is significantly brighter than the counter jet both on-axis and at the edge of the jet (Canvin et al. 2005).

We successfully fit the structure of the inner ±70 arcsec of the jets in NGC 315 using an intrinsically symmetrical model in which all apparent differences between the main and counter jets result from relativistic aberration and beaming (Canvin et al. 2005). Such models clearly cannot be continued to indefinitely large scales, as FRI jets almost always show evidence (e.g. bends and disruption) for asymmetric interaction with the external medium. The largest-scale structure of NGC 315 shown in Fig. 1(a) is an excellent example, with jets of unequal length terminating in entirely different ways. This raises the question: how large is the region over which symmetrical, relativistic models can be applied? At 400 arcsec from the nucleus, there are clear asymmetries in both the deflection and collimation properties; these must be intrinsic, although the overall brightness asymmetry persists. There is also good evidence for interaction with the external medium at distances of 70–100 arcsec on both sides of the nucleus, where both jets bend (symmetrically, this time). It seems likely that intrinsic and relativistic effects become comparable between 100 and 200 arcsec, where the sidedness difference on-axis is the same as on small scales, but the edge value is reversed. Asymmetries in apparent magnetic field structure, which also imply that the flow remains mildly relativistic in this region, are discussed in Section 6. Our working hypothesis is therefore that relativistic effects dominate the observed differences between the two jets only before the first bends, but that environmental effects become first comparable and then dominant at larger distances, although slightly relativistic bulk flow probably continues to the largest scales and may remain responsible for the generally brighter appearance of the NW jet far from the nucleus.

4 SPECTRA

4.1 Accuracy

We define spectral index α in the sense $S(\nu) \propto \nu^{-\alpha}$. We estimated spectral indices both for individual pixels and by integration of flux density over well-defined regions. Values at 5.5-arcsec resolution were determined from weighted power-law fits to data at all five frequencies between 1.365 and 5 GHz. At 1.5-arcsec resolution, spectral indices were calculated between 1.413 and 5 GHz.

There are three main sources of error in the estimate of α as follows.

(i) The transfer of the amplitude scale from the primary calibrator. The errors for the four *L*-band frequencies are likely to be tightly correlated, since they were observed during the same periods, data being taken simultaneously at 1365 and 1413 MHz, and at 1485 and 1665 MHz. Consequently, the principal effect of flux-density scale transfer errors is a constant offset in spectral index.

(ii) Residual deconvolution effects, typically on scales of 5–20 arcsec. These are approximately proportional to surface brightness.

(iii) Thermal noise.

We model the error from (ii) as 0.03 times the flux density and that from (iii) as the noise level estimated off-source (from Table 3), appropriately integrated. These two contributions are added in quadrature. In addition, we estimate the rms spectral-index offset due to transfer errors in the flux-density scale to be 0.02. This should be taken in addition to the errors quoted below.

4.2 Spectral-index images and tomography

Figs 5(a) and (b) show the spectral indices, α, determined from a weighted power-law fit to data at all five frequencies between 1.365 and 5 GHz at 5.5-arcsec resolution and between 1.413 and 5 GHz at a resolution of 1.5 arcsec, respectively.

It is clear from Fig. 5(a) that there are transverse gradients in spectral index where the jets are expanding rapidly. These gradients can only be seen clearly on spectral-index images where the errors are small, and for this reason both panels of Fig. 5 are blanked where the rms error in α is >0.05. In order to search for transverse variations over a larger area, we need to average along the jets. The gradients between 34.5 and 69 arcsec from the nucleus are best displayed by averaging along radii from the nucleus and plotting the results against angle from the local jet axis, as is shown for the main and counter jets in Fig. 6(a). Further from the nucleus, where the jets recollimate, we have averaged along the local jet axis to derive transverse spectral-index profiles. The results are shown for two regions in each of the main and counter jets in Fig. 7. The fluctuations in these regions are dominated by quasi-periodic deconvolution errors: this problem is particularly acute for the counter jet at $\sim$100 arcsec from the nucleus (Fig. 7a). The spectral index is everywhere consistent with the mean value of $\langle\alpha\rangle = 0.47$ between 70 and 160 arcsec.

Another method of displaying spatial variations of the spectrum is 'spectral tomography' (Katz-Stone & Rudnick 1997; Katz-Stone et al. 1999). This involves the generation of a set of images $I_t(\boldsymbol{r}) = I(\boldsymbol{r},\nu_1) - (\nu_2/\nu_1)^{\alpha_t} I(\boldsymbol{r},\nu_2)$ for a range of values of α_t, where $I(\boldsymbol{r}, \nu)$ is the brightness at position $\boldsymbol{r}$ and frequency ν. If the brightness distribution can be represented as the sum of two components with different spectral indices $I(\boldsymbol{r},\nu) = S_a(\boldsymbol{r})\nu^{-\alpha_a} + S_b(\boldsymbol{r})\nu^{-\alpha_b}$, then the 'a' component will disappear from the image I_t when $\alpha_t = \alpha_a$. We made a set of images of I_t with $\nu_1 = 1.365$ GHz, $\nu_2 = 5$ GHz and α_t from 0.4–0.7 in steps of 0.01. For $\alpha_t \approx 0.44$, the outer edges of both jets disappear at distances from the nucleus between $\approx$22 and 80 arcsec. The image of I_t for $\alpha_t = 0.44$ is shown in Fig. 8. Further from the nucleus, I_t is close to zero across the whole width of both jets for $\alpha_t \approx 0.47$. There is no single value of α_t for which the steep-spectrum component vanishes completely in an image of I_t.

The main features of the spectral-index distribution are as follows.

(i) Variations in the spectral index are subtle ($0.4 \lesssim \alpha \lesssim 0.65$ everywhere).

(ii) The spectral index is slightly, but significantly steeper in the jet bases than elsewhere. Between 7.5 and 22.5 arcsec from the nucleus the mean values at 5.5-arcsec resolution are 0.63 and 0.58 in the main and counter jets, respectively (the difference between them is not significant).

(iii) At 1.5-arcsec resolution (Fig. 5b), the spectral index of the main jet is essentially constant for the first $\approx$15 arcsec, with a mean spectral index $\langle\alpha\rangle = 0.61$, consistent with the value determined at lower resolution.

(iv) Between $\approx$15 and 70 arcsec from the nucleus, the spectral index is steeper on-axis ($\alpha \approx 0.5$) than at the edges ($\alpha \approx 0.44$) in both jets. This is illustrated by the transverse profiles averaged between 34.5 and 69 arcsec from the nucleus (Fig. 6a).

(v) At 1.5-arcsec resolution, the on-axis spectral index is slightly higher between 15 and 60 arcsec from the nucleus ($\langle\alpha\rangle = 0.55$;

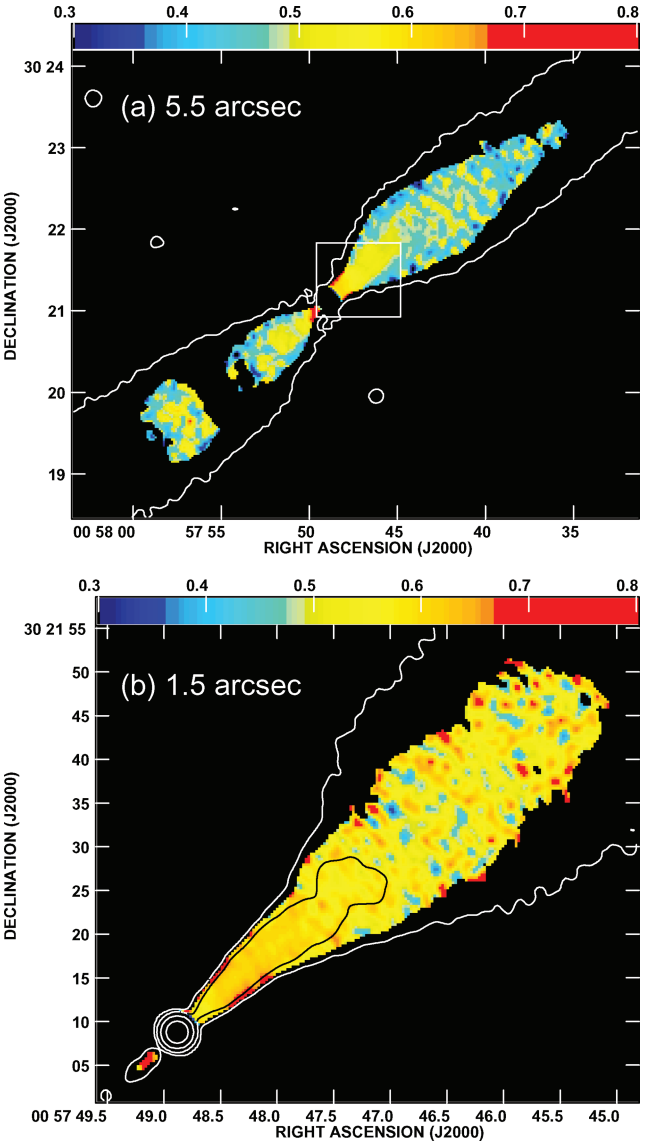

Figure 5. (a) False-colour plots of spectral index, α, over the range 0.3–0.8. (a) α determined by weighted power-law fits to data at all five frequencies between 1.365 and 5 GHz. The resolution is 5.5 arcsec FWHM. Data are plotted only where the rms error in α (excluding flux-density scale offsets) is <0.05 and the signal-to-noise ratio at all frequencies is >5. All of the images were made using a zero-spacing flux density and the (small) residual zero-point offsets were subtracted before fitting. The 75 μJy (beam area)$^{-1}$ contour from the mean L-band I image is also plotted. (b) α between 1.413 and 5 GHz at a resolution of 1.5 arcsec FWHM for the area shown by the box in panel (a). Data are plotted only where the rms error in α (again excluding flux-density scale offsets) is <0.05 and the difference between estimates of α before and after zero-level subtraction <0.01. Representative contours of total intensity at 5 GHz are also plotted.

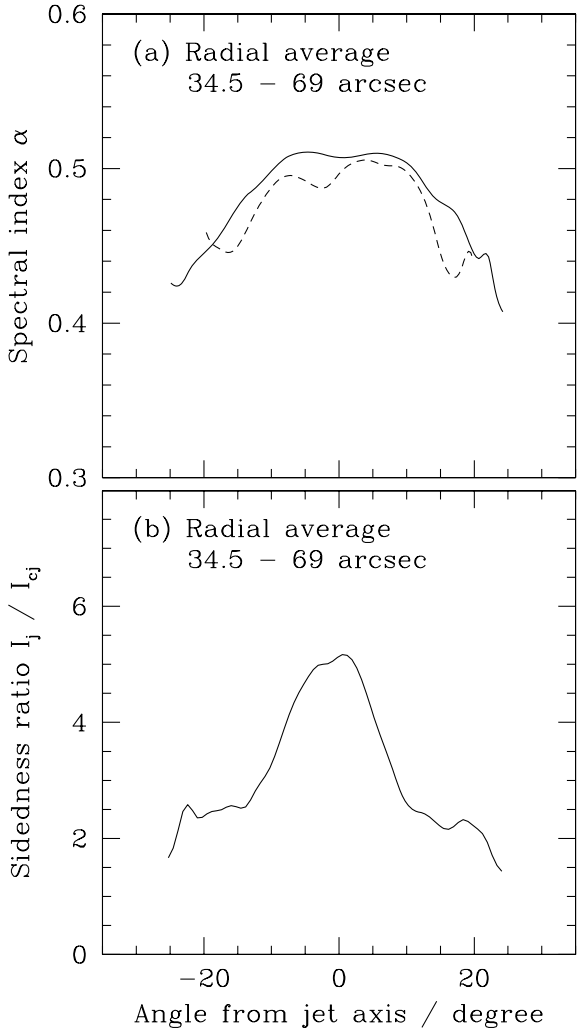

Figure 6. (a) Averaged transverse profile of the spectral index determined from a weighted power-law fit to data at all five frequencies between 1.365 and 5 GHz, as in Fig. 5(a). The resolution is 5.5 arcsec FWHM. The data were averaged along radii from the nucleus between 34.5 and 69 arcsec and are plotted against angle from the jet axis, here taken to be in position angle $-48\overset{\circ}{.}5$. Full curve: main jet, dashed curve: counter jet. (b) Profile of jet/counter-jet sidedness ratio, from the data in Canvin et al. (2005), averaged as in panel (a), but with a resolution of 2.35 arcsec FWHM.

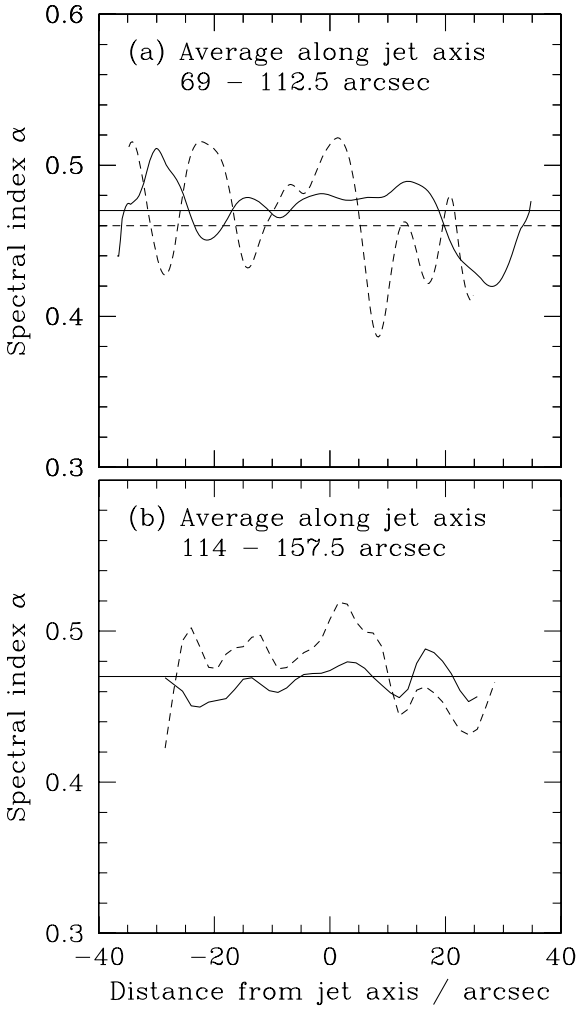

Figure 7. Averaged transverse profiles of the spectral index determined from weighted power-law fits to data at all five frequencies between 1.365 and 5 GHz, as in Fig. 5(a). The resolution is 5.5 arcsec FWHM. The data were averaged along the local jet axis, taken to be in position angle $-52\overset{\circ}{.}8$. Full curve: main jet; dashed curve: counter jet. The horizontal lines indicate the mean spectral indices for the regions, which are close to 0.47 in all cases. (a) 69–112.5 arcsec, determined by averaging the spectral-index image. (b) 114–157.5 arcsec, determined by summing individual I images and making weighted power-law fits (the spectral-index image is too noisy to be averaged towards the jet edges).

Fig. 5b) than at smaller distances. α cannot be determined to adequate accuracy at the edges of the jet for distances $\gtrsim$15 arcsec at this resolution.

(vi) The tomographic analysis shows the spectral gradient in a different way: if we subtract off a component with $\alpha_t = 0.44$ (Fig. 8), the emission at the edges of the jet and at large distances from the nucleus essentially vanishes. What remains (positive in Fig. 8) corresponds to the jet bases and to a ridge of steeper-spectrum emission at larger distances. The latter is clearly visible in both jets.

(vii) The flatter-spectrum edge first becomes detectable at $\approx$15 arcsec from the nucleus and widens thereafter. It occupies the entire width of the jet from $\approx$70 arcsec outwards. The transition between steeper and flatter spectrum on-axis is poorly defined.

(viii) There is no evidence for any transverse spectral gradient at larger distances, after the jets recollimate, although the data are noisy and do not cover quite the full width of the jets (Fig. 7).

(ix) This is confirmed by the tomographic analysis: I_t for the outer parts of the region vanishes for $\alpha_t = 0.47$, the mean spectral index, confirming that α is constant within our errors.

4.3 Deprojection of the spectral-index distribution

Katz-Stone et al. (1999) and Katz-Stone & Rudnick (1997) suggested that the spectral index of an *on-axis* component in a jet is the value of α_t at which the component appears to vanish against the background of the surrounding emission (exactly as for an *edge* component such as that in the NGC 315 jets; Section 4.2) and can therefore be derived simply from a tomographic analysis. This requires an additional assumption which may not be correct, namely that when the on-axis component is subtracted, the remaining emission has a smooth brightness distribution (this is *not* true for the model proposed below). For NGC 315, our three-dimensional model of the emissivity (Canvin et al. 2005) gives a good fit to the observed

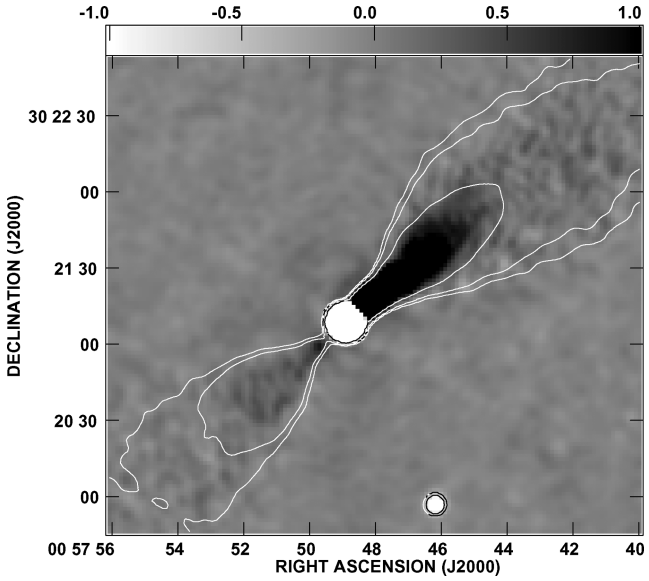

Figure 8. The grey-scale plot shows a difference image $I(\nu_1) - (\nu_2/\nu_1)^{\alpha_t} I(\nu_2)$ for $\nu_1 = 1.413$ GHz, $\nu_2 = 5$ GHz and $\alpha_t = 0.44$ over the range -1 to $+1$ mJy (beam area)$^{-1}$. The resolution is 5.5 arcsec FWHM. A few contours of the 5 GHz I image are superposed to outline the jet structure.

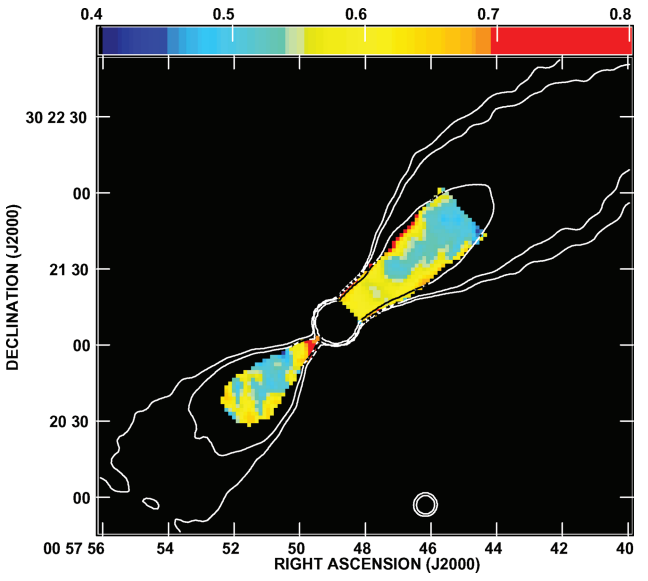

Figure 9. The false-colour plot shows an estimate of the spectral index for the on-axis emission component alone in the range $0.4 \leqslant \alpha \leqslant 0.8$. The spectral-index distribution is truncated at a distance of 66.5 arcsec along the axis and is shown only where the residual surface brightnesses exceed 0.5 and 1 mJy (beam area)$^{-1}$ at 5 and 1.365 GHz, respectively. A few contours of the 5 GHz I image are superposed to outline the jet structure. The area covered is the same as that in Fig. 8 and the resolution is 5.5 arcsec FWHM.

emission at 5 GHz, so we isolated the on-axis component and measured its spectral index, as follows.

(i) We first used the tomography image with $\alpha_t = 0.44$ as a template for the on-axis component. To a reasonable approximation, this defines a cone with a half-opening angle of 13.°6 projected on the sky. Assuming an angle to the line of sight of $\theta = 38°$ (Canvin et al. 2005), the half-opening angle in the jet frame is 8.°3.

(ii) We then made a model 5-GHz image, as in Canvin et al. (2005) but with the emissivity set to zero within this cone, convolved it to a resolution of 5.5 arcsec and subtracted it from the observed 5-GHz I image. The residual corresponds to the observed emission from within the central cone.

(iii) We scaled the model to 1.365 GHz assuming a spectral index of 0.44, as appropriate for the edge emission and then subtracted it from the observed 1.365-GHz image.

(iv) Both residual images showed little emission towards the edges of the jets, implying that the model subtraction was reasonably accurate.

(v) Finally, we derived a spectral-index image for the on-axis component alone. This is shown in Fig. 9.

Fig. 9 shows that the spectrum of the on-axis component flattens slightly with distance from the nucleus. The mean values of α between 7.5 and 22.5 arcsec are 0.60 and 0.61 for the main and counter jets, respectively. The corresponding values for distances between 22.5 and 66.5 arcsec are 0.56 and 0.55. For the main jet, these values are consistent with the measurements at 1.5-arcsec resolution without subtraction. At 5.5-arcsec resolution in both jets, they are slightly higher than the values measured on-axis before subtraction, which include a contribution from the flatter-spectrum, off-axis component. We conclude that the structure observed in Fig. 5(a) does not result entirely from the superposition of two components with constant, but different spectral indices. The sketch in Fig. 10 summarizes our results on the distribution of spectral index in the jets.

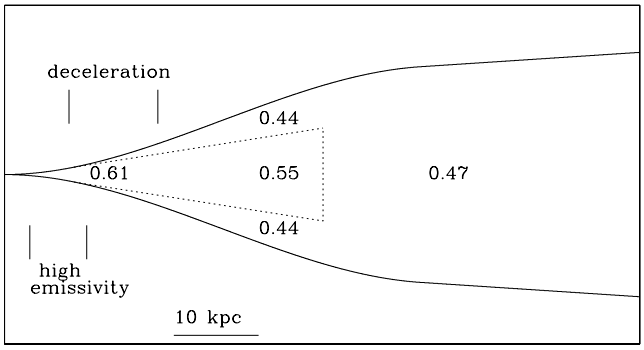

Figure 10. A sketch of our proposed three-dimensional distribution of spectral index in the jets of NGC 315. The sketch is in a plane containing the jet axis, assuming an angle to the line of sight of 37.°9 (Canvin et al. 2005) and a linear scale is given. 10 kpc along the jet projects to 18 arcsec on the plane of the sky. The values of α at various points in the jet are marked, together with the approximate extent of the steep-spectrum component (dotted) and the regions of high emissivity and rapid deceleration (Canvin et al. 2005).

4.4 Comparison with other sources

Typical spectral indices for the flaring regions of other FRI radio jets are in the range 0.5–0.6 (Young et al. 2005 and references therein). Indeed, Young et al. (2005) suggested that FRI jets have a 'canonical' low-frequency spectral index of $\alpha = 0.55$, but this conclusion is based primarily on lower-resolution data than we consider here. Their canonical value is intermediate between that for the jet bases in NGC 315 and the significantly flatter spectra seen at larger distances.

There are very few published studies of spectral *variations* in the flaring regions of FRI jets. Short regions of slightly steeper spectrum than the average have been detected in the bases of three other FRI jets: 3C 449 (Katz-Stone & Rudnick 1997), PKS 1333−33 (Killeen,

Bicknell & Ekers 1986) and 3C 31 (Laing et al., in preparation). The measurement of $\alpha = 0.7 \pm 0.2$ in 3C 449 applies to the faint inner jets (corresponding to the innermost 5 arcsec in NGC 315), but differs marginally from that of the brighter nearby emission, given the large error. In PKS 1333−33, the spectrum flattens from $\alpha \approx 1.0$ to $\alpha \approx 0.6$ between 10 and 35 arcsec from the nucleus (2.4–8.4 kpc in projection); this includes both the faint inner jets and the bright part of the flaring region, as in NGC 315. In 3C 31, there is a steeper-spectrum region extending to ≈6 arcsec in the main jet (plausibly also in the counter jet).

There is a flatter-spectrum edge on one side of the main jet in 3C 31 (Laing et al., in preparation). Transverse variations of spectral index in the sense that the spectrum is *steeper* on-axis have not been reported in any other sources, but their flaring regions are smaller in both linear and angular size and are difficult to resolve. Gradients at the level of $\Delta\alpha \approx 0.05$–$0.1$ are also tricky to detect without data at more than two frequencies.

The tendency for the jet spectrum to be flatter at the edge is in the opposite sense to the spectral gradients found on large scales in tailed radio sources (Katz-Stone & Rudnick 1997; Katz-Stone et al. 1999, Laing et al., in preparation) but the latter effect occurs in completely different regions of the jets, where they merge into the tails.

4.5 Acceleration mechanisms

The X-ray emission detected by Worrall et al. (2003) in NGC 315 coincides with the steeper-spectrum ($\alpha = 0.61$) region at the base of the main jet. The form of the synchrotron spectrum in those FRI jet bases which emit X-rays is now well established (Hardcastle, Birkinshaw & Worrall 2001; Hardcastle et al. 2002; Parma et al. 2003; Hardcastle et al. 2005; Perlman & Wilson 2005). It can be characterized as a broken power law with spectral indices of 0.5–0.6 at radio wavelengths and 1.2–1.6 in X-rays. The spectrum of NGC 315 is consistent with this pattern, although its high-frequency slope is poorly constrained (Worrall et al. 2003). This spectral shape is consistent with synchrotron emission from a single electron population; ongoing particle acceleration is therefore required (see also Worrall et al., in preparation). The magnetic field strengths calculated for the on-axis emissivity model of Canvin et al. (2005), assuming a minimum-pressure condition, range from 3.3 nT at 6 arcsec in projection to 0.44 nT at 69 arcsec. For electrons with Lorentz factor γ radiating at the synchrotron critical frequency ν_c in a magnetic field B, we have $\nu_c/\mathrm{Hz} = 41.99\,\gamma^2\,(B/\mathrm{nT})$ (Longair 1994), so at 5 GHz, $6 \times 10^3 \lesssim \gamma \lesssim 1.6 \times 10^4$ and in the X-ray band at 1 keV, $4 \times 10^7 \lesssim \gamma \lesssim 1.1 \times 10^8$.

The flatter-spectrum edges occur where Canvin et al. (2005) infer substantial velocity shear across the jets. If the jets are relativistic and faster on-axis than at their edges, the approaching jet always appears more centre-brightened than the receding one. This difference is reflected in the sidedness-ratio image. The average transverse sidedness profile between 34.5 and 69 arcsec from the nucleus is shown in Fig. 6(b) for comparison with the spectral-index profile over the same region. The velocity profile is modelled as a truncated Gaussian function with $\beta = 0.38$ on-axis and 0.22 at the edge, although Canvin et al. (2005) note that the on-axis velocity may be larger ($\beta \approx 0.5$) if the shear occurs over a narrow range of radii in the jet: this might give a better fit to the sidedness profile.

The flatter-spectrum edge first becomes visible ≈15 arcsec from the nucleus. This coincides to within the errors with

(i) the *start* of rapid deceleration, as inferred by Canvin et al. (2005), 14 arcsec in projection from the nucleus;

(ii) the *end* of the region of enhanced radio and (in the main jet only) X-ray emissivity (Canvin et al. 2005, Worrall et al., in preparation);

(iii) the first point at which the observed jet/counter-jet sidedness image gives any evidence for transverse velocity gradients, 16 arcsec from the nucleus (Canvin et al. 2005).

The deceleration and enhanced emission regions are marked in Fig. 10. Note that the detection of transverse gradients in sidedness and spectral index may be limited by resolution.

The changes of spectral index observed in NGC 315 suggest that (at least) two different electron-acceleration mechanisms are required, as follows.

(i) The first mechanism dominates at the base of the flaring region (the initial 15 arcsec in NGC 315) and may continue at a lower level on the axis of the jet to ≈70 arcsec. It generates emission from radio to X-ray wavelengths and has a characteristic spectral index $\alpha \approx 0.6$ in the former band. Three pieces of evidence suggest that this mechanism is dominant where the jet is fast ($\beta \approx 0.9$). First, its characteristic spectral index is observed across the whole of the jet width in NGC 315 until the start of rapid deceleration. Secondly, in both 3C 31 (Laing & Bridle 2004) and NGC 315 (Worrall et al. 2003), the bright X-ray emission occurs upstream of the deceleration region. Finally, Laing & Bridle (2004) show from radio data alone that significant injection of fresh relativistic particles is required before the start of deceleration in 3C 31 to counter-balance adiabatic losses.

(ii) The second mechanism causes the flattening of the spectrum towards the edges of the jets observed from 15 arcsec outwards, but eventually spreading over the entire jet width. It produces spectral indices in the range $0.44 \lesssim \alpha \lesssim 0.5$ for electrons emitting at radio wavelengths in NGC 315 and appears to be associated with velocity shear across the jets. A possible candidate for the this mechanism is the shear acceleration process described by Rieger & Duffy (2004, 2005), but their estimates of the acceleration time-scale for electrons in conditions appropriate to FRI jets are very long (at least if the mean free path ∼ gyro-radius), and it is unclear whether the process is efficient enough to influence the spectrum.

5 FARADAY ROTATION AND DEPOLARIZATION

5.1 Faraday rotation

In order to investigate the variations of Faraday rotation along the jets of NGC 315, we made images of rotation measure (RM) at a resolution of 5.5 arcsec by least-squares fitting to the relation $\chi(\lambda^2) = \chi(0) + \mathrm{RM}\,\lambda^2$ (where χ is the $\boldsymbol{E}$-vector position angle) for all five frequencies between 1.365 and 5 GHz. The fits were weighted by errors in χ derived from Table 3. We excluded a small region around the core which was affected by residual instrumental polarization and included only points where the rms error in position angle was $<15^\circ$ at all frequencies. The resulting RM image is shown in Fig. 11(a). The fit to a λ^2 law is very good everywhere: two examples are shown in Fig. 12. The extreme value of $\mathrm{RM} \approx -90\,\mathrm{rad\,m^{-2}}$ results in rotations of $\approx 1^\circ$ between the two centre frequencies combined in our 5-GHz data set and $\approx 0\overset{\circ}{.}4$ and $\approx 5^\circ$ across the bands at 5 and 1.4 GHz, respectively. The worst of these effects, rotation across the band at the lowest frequencies, results in a spurious depolarization <0.1 per cent, which is negligible compared with errors due to noise. The images of Q and U show little power on large spatial scales and our estimates of position angle should be reliable

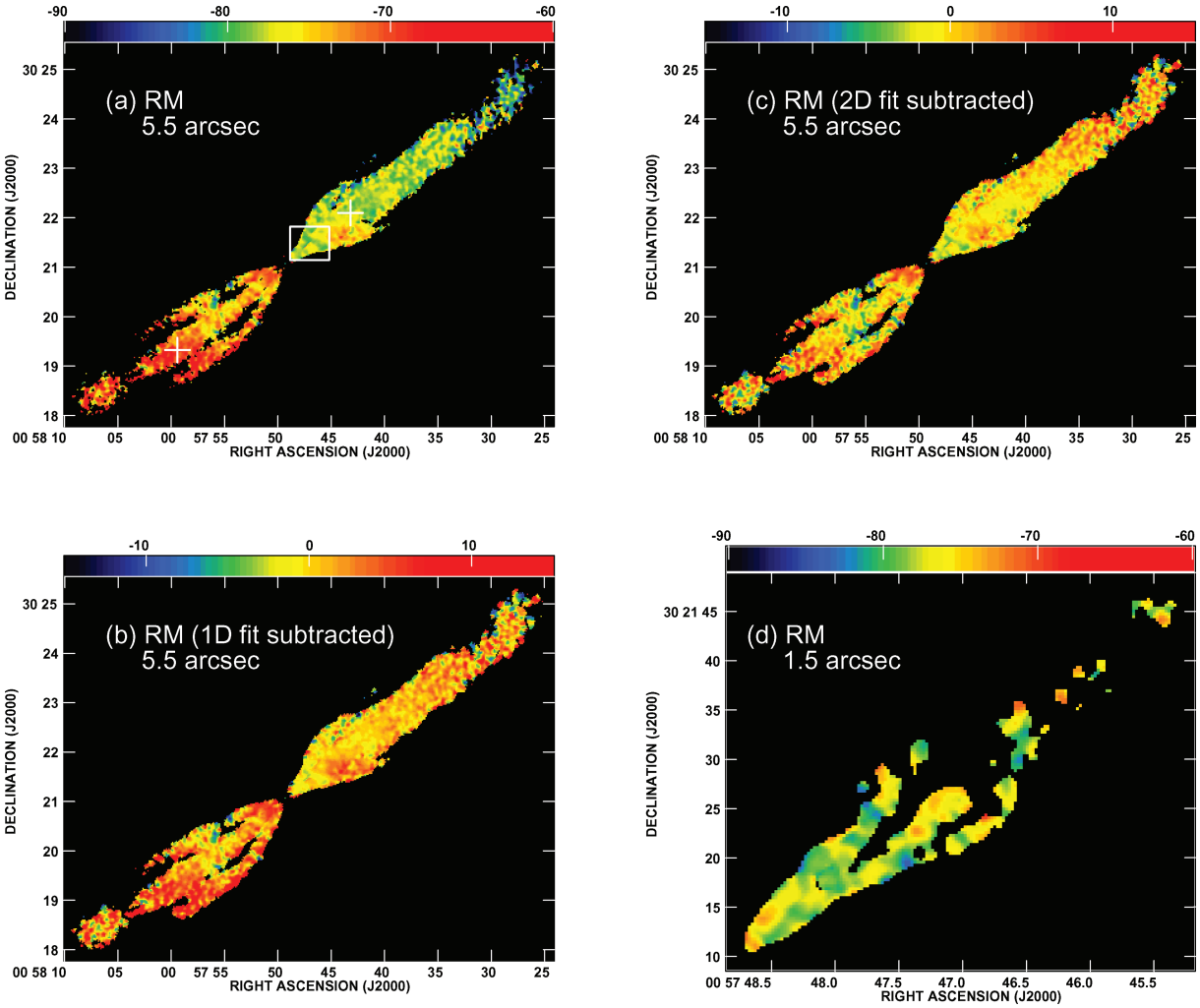

Figure 11. False-colour images of RM for the jets in NGC 315. In panels (a)–(c), the RM is derived from fits to ***E***-vector position angles at five frequencies. (a) Observed RM, in the range −90 to −60 rad m^{-2}. The crosses mark the positions corresponding to the $\chi - \lambda^2$ plots in Fig. 12. (b) RM after subtraction of a linear function of distance along the jet derived from an unweighted fit to the data in the range −15 to +15 rad m^{-2}. (c) As (b), but for a fit to gradients along and across the jets. (d) RM at a resolution of 1.5 arcsec FWHM, derived from the position-angle difference between 1.413 and 5 GHz, using the lower-resolution RM image to resolve $n\pi$ ambiguities. Data are plotted only where the rms error in RM <2 rad m^{-2}. The area covered by this figure is indicated by the box on panel (a).

over the full range of distances from the nucleus shown in Fig. 11(a). The area over which the RM can be determined accurately is limited primarily by the primary beam at 5 GHz (540 arcsec FWHM).

The mean RM is −75.7 rad m^{-2}. The most obvious feature of the RM image is a nearly linear gradient along the jets, as shown by the profile in Fig. 13(a). In order to reveal smaller-scale structure in the RM, we initially fitted and subtracted a function $\mathrm{RM} = \mathrm{RM}_0 + a_x x$, where x is measured along the axis from the nucleus (a_x and RM_0 are constants). We used an unweighted least-squares fit, as any attempt to weight by the estimated errors caused the brightest part of the main jet to be fitted at the expense of other regions. The gradient is $a_x = 0.025$ rad m^{-2} arcsec^{-1} and the residual image is shown in Fig. 13(b). This indicates that variations in RM across the jet are also significant, as can be seen more clearly in averaged profiles, particularly between 69 and 112.5 arcsec from the nucleus (Fig. 14b). Closer to the nucleus, the gradient is barely visible (Fig. 14a), but the jets are narrower there and the profiles are consistent with the gradient measured at larger distances. The transverse variation also appears to be linear, so we fitted and subtracted a function $\mathrm{RM} = \mathrm{RM}_0 + a_x x + a_y y$, where y is a coordinate transverse to the jet and a_y is a constant. The gradients along and transverse to the jet axis become $a_\mathrm{x} = 0.018$ rad m^{-2} arcsec^{-1} and $a_\mathrm{y} = 0.051$ rad m^{-2} arcsec^{-1}, respectively. Taken at face value, the best-fitting gradient is 0.054 rad m^{-2} arcsec^{-1} at an angle of 72° to the mean jet axis. Note, however, that the transverse gradient is essentially determined by a subset of the data from the widest parts of the main and counter jets (Fig. 14b).

Removal of the large-scale gradient leaves fluctuations in the local mean RM which appear significantly larger on the counter-jet side (Fig. 11c). By definition, the signal-to-noise ratio in I is lower in the counter jet. Although this is partially offset by a higher average degree of polarization, the errors in RM are still larger than in the main jet. To evaluate the significance of the fluctuations, we considered only points with fitting errors $\leqslant$2.5 rad m^{-2} and calculated the expected errors in the means for boxes of length 30 arcsec along the jet axis containing more than 50 such points (the errors are corrected for oversampling). The results are shown in Fig. 13(b). The fluctuations are significant, and form an ordered pattern with a

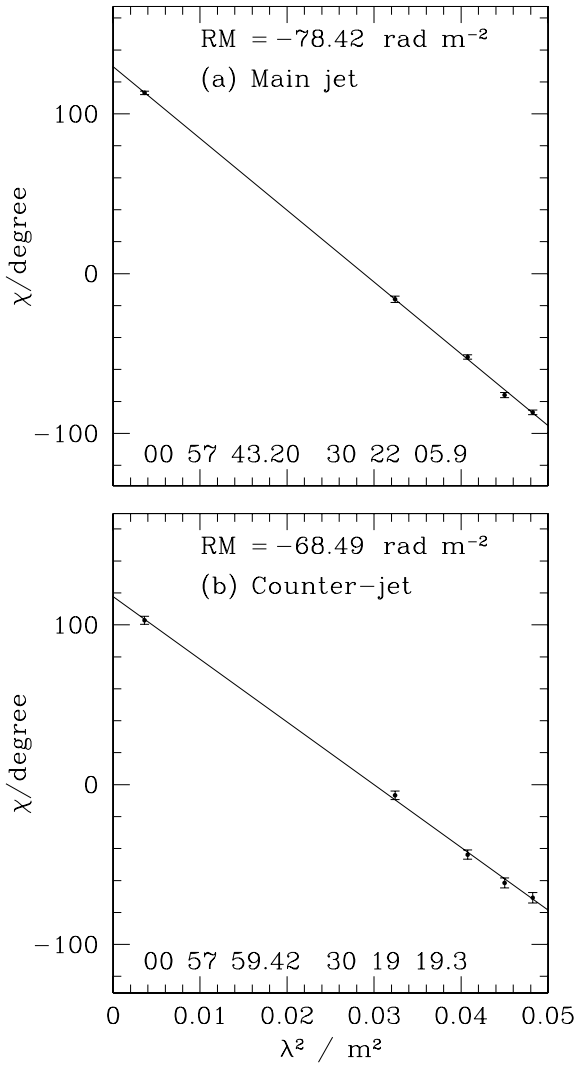

Figure 12. Plots of $\boldsymbol{E}$-vector position angle, χ, against λ^2 for representative positions in the main jet (panel a) and counter jet (panel b). The coordinates are given on the plots and the positions are those marked by crosses in Fig. 11(a).

typical scale ∼100 arcsec. They are larger by a factor of ≈2 in the counter jet and the first bin of the main jet (within 30 arcsec of the nucleus) compared with the rest of the main jet.

The residual fluctuations within the boxes (i.e. after subtracting the local mean) are comparable with the errors in RM except in the brightest regions close to the nucleus. We therefore made a first-order correction to the rms RM, $\sigma_{\rm RMraw}$, by subtracting the fitting error $\sigma_{\rm fit}$ in quadrature to give $\sigma_{\rm RM} = (\sigma^2_{\rm RMraw} - \sigma^2_{\rm fit})^{1/2}$. The profiles of $\sigma_{\rm RMraw}$ and $\sigma_{\rm RM}$ are both plotted in Fig. 13(c), for the same selection of points as in Fig. 13(b). The corrected profile is very uncertain, but suggests that $\sigma_{\rm RM}$ has a maximum of 2 rad m^{-2} close to the nucleus on the counter-jet side and may be slightly asymmetric in the sense that the rms RM is lower in the main jet than the counter jet at the same distance from the nucleus.

We can image these smaller-scale fluctuations directly only at the bright base of the main jet. There, the RM at a resolution of 1.5 arcsec FWHM can be derived accurately from the difference between 1.413 and 5 GHz position-angle images, using the lower-resolution data to resolve the $n\pi$ ambiguity. Fig. 11(d) shows the

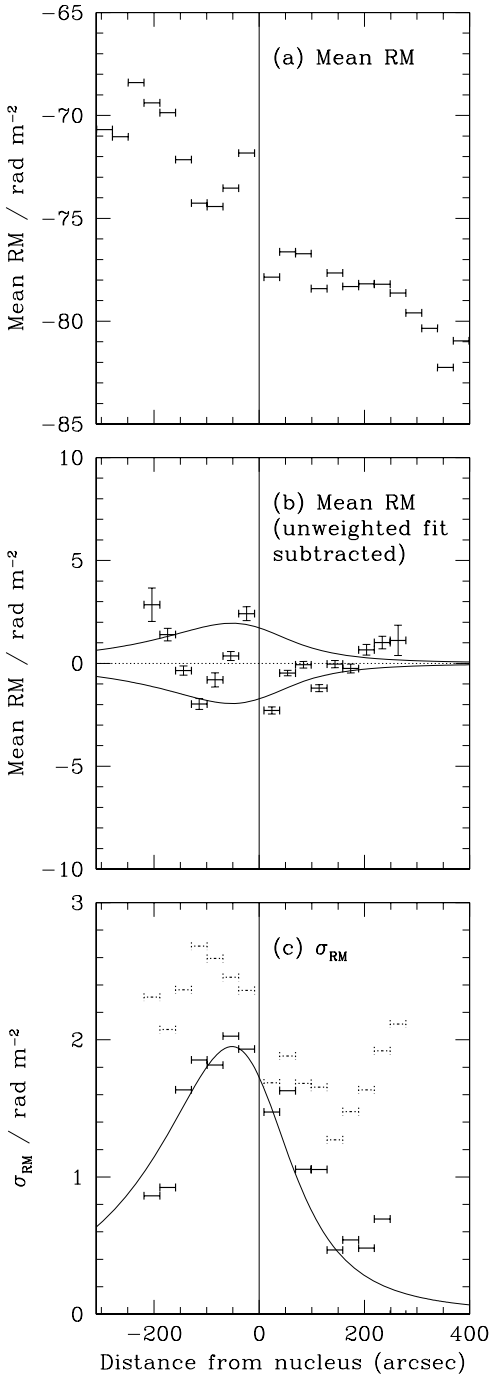

Figure 13. Variation of the mean and rms RM along the jets. The average jet axis is taken to be at position angle −52°.8. (a) A profile of RM averaged over boxes of length 30 arcsec along the jet axis. (b) Mean RM profile, after subtraction of a linear fit. Only points with fitting error $\leqslant$2.5 rad m^{-2} were used and boxes are only plotted if they contain more than 50 such points. The vertical bars indicate the error on the mean. (c) The rms RM, with respect to the mean of the points in the box. Dashed bars denote the uncorrected values, $\sigma_{\rm RMraw}$; full bars show the values after making a first-order correction for fitting error, $\sigma_{\rm RM}$ (see text). The curve plotted in panels (b) and (c) is the model rms RM profile described in the text.

RM at this resolution. Data are plotted only where the rms error in the fitted RM <2 rad m^{-2}. Fluctuations are clearly detected: the rms is $\sigma_{\rm RMraw} = 2.1$ rad m^{-2}, giving $\sigma_{\rm RM} = 1.6$ rad m^{-2} after making a first-order correction for fitting error, as above. This is in good

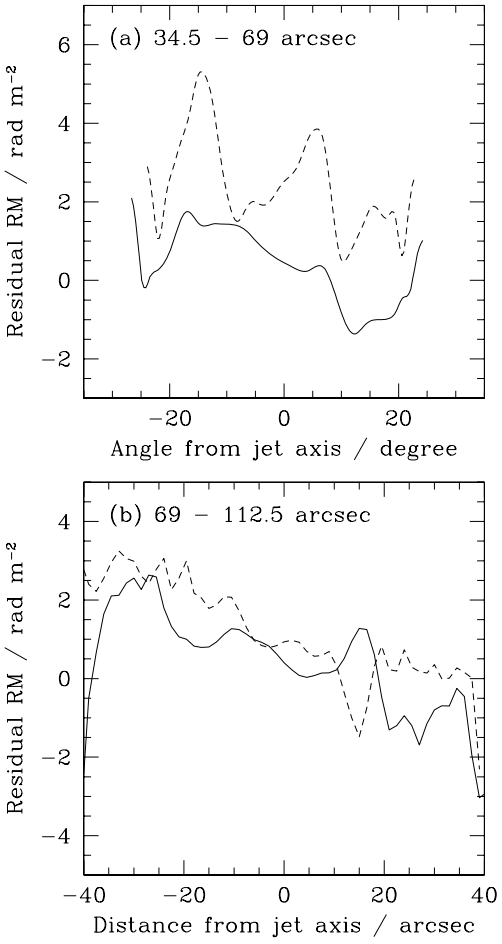

Figure 14. Transverse variation of RM after subtracting a uniform gradient along the axis for the main jet (full line) and counter jet (dashed line). (a) Averages along radii from the nucleus between 34.5 and 69 arcsec plotted against the angle from the axis, which is taken to be in position angle $-48\overset{\circ}{.}5$. (b) Averages along the jet (in position angle $-52\overset{\circ}{.}8$) between 69 and 112.5 arcsec, plotted against distance from the axis.

agreement with the value for the innermost bin of the profile of rms RM for the main jet at lower resolution (Fig. 13c).

5.2 Depolarization

The variation of p with wavelength at low resolution potentially measures fluctuations of RM across the observing beam which cannot be imaged directly with adequate sensitivity. This variation is small, and is best quantified by fitting to the first-order approximation $p(\lambda^2) \approx p(0) + p'(0)\lambda^2$ where $p'(\lambda^2) = \mathrm{d}p/\mathrm{d}(\lambda^2)$. We expect $p'(0) < 0$ (depolarization) under most circumstances. The quantity $p'(0)/p(0)$ is directly related to the commonly quoted depolarization ratio, but is biased in the present case, since both the gradient and the degree of polarization depend directly on a single high-frequency measurement (at 5 GHz), so deviations in $p(0)$ and $p'(0)$ are anticorrelated. We therefore tested for the presence of depolarization using the gradient $p'(0)$ alone. We derived $p'(0)$ by weighted least-squares fitting to images of p at the five frequencies between 1.365 and 5 GHz at a resolution of 5.5 arcsec FWHM. Two sets of p images were used: in the first, an estimate of the local zero level was subtracted from the I images before calculating $p = P/I$; in the second, the original I images were used (any differences indicate systematic errors in the estimation of large-scale structure). The fitting weights were the inverse squares of errors in p derived from the values in Table 3 and points were only included if the errors were <0.3 at all frequencies. The resulting polarization gradients are very small, and there are no obvious variations. In order to determine the significance of the gradients, we measured their mean values over the main and counter jets. The maximum scale of structure imaged accurately in total intensity is $\approx$300 arcsec (Table 2), so we calculated the means for points between 9 and 150 arcsec from the nucleus along the jet axis (excluding the small region around the core to avoid spurious instrumental polarization, as in Section 5.1). The mean values for the main and counter jets derived from the zero-level corrected images were $\langle p'(0)\rangle = 0.03 \pm 0.08$ and 0.16 ± 0.16, respectively. Without zero-level correction, the values become 0.05 ± 0.08 and 0.22 ± 0.16. We conclude that the increase of p with wavelength for $\lambda \leqslant 0.22$ m ($\nu \geqslant 1.365$ GHz), which is in any case opposite to the expected effects of Faraday rotation, is not significant.

5.3 The origin of the rotation measure

NGC 315 has Galactic coordinates $l = 124\overset{\circ}{.}6$, $b = -32\overset{\circ}{.}5$. This is on the outskirts of region A of Simard-Normandin & Kronberg (1980), where the majority of sources have large negative RMs (~ -100 rad m^{-2} at the centre of the region). Dineen & Coles (2005) derived spherical-harmonic models of the Galactic RM distribution by fitting to RMs of large numbers of extragalactic sources. These models predict a Galactic contribution ≈ -47 rad m^{-2} at the position of NGC 315. The bulk of the mean RM of -75.7 rad m^{-2} is therefore likely to be Galactic in origin.

Simonetti & Cordes (1986) determined RM variations, which they argued to be primarily Galactic, across a number of sources within region A (their region 1). Their plot of squared RM difference $\Delta\mathrm{RM}^2$ against separation suggests $\langle\Delta\mathrm{RM}^2\rangle^{1/2} \sim 10$–30 rad m^{-2} on a scale of 700 arcsec, but with large uncertainties. The observed ΔRM ($\approx$15 rad m^{-2} on the same scale along the jets of NGC 315; Fig. 13a) is again consistent with a Galactic origin. The maximum change in RM across the jet ($\approx$4 rad m^{-2} over 80 arcsec; Fig. 14b) is within the range of the upper limits plotted by Simonetti & Cordes (1986). We note, however, that NGC 315 is located outside the core of region A, so it may be that smaller values of $\langle\Delta\mathrm{RM}^2\rangle^{1/2}$ are appropriate.

The linearity of the RM gradient along the jet and the fact that the maximum gradient is aligned neither with the jet axis nor with the minor axis of the galaxy both imply that little of the Faraday rotating medium is associated with the jets or with the host galaxy. In either case, we would expect some non-linear variation with distance from the nucleus.

We conclude that most of the mean RM and its linear gradient are likely to be Galactic in origin, but a significant contribution from material local to NGC 315 is not ruled out. In particular, we cannot exclude the hypothesis that some of the RM gradient transverse to the jet results from an ordered toroidal field within or just outside the jet (Laing 1981; Blandford 1993). The associated position angle rotation between 1.365 and 5 GHz is at most a few degrees and significant departures from λ^2 rotation would not be detectable even if the thermal plasma responsible for the Faraday rotation is mixed with the synchrotron-emitting material (Burn 1966). If local toroidal fields are solely responsible for the transverse RM gradients, then their vector directions must be the same in the main and counter jets.

The *residual* RM fluctuations are qualitatively very similar to those in 3C 31 (Laing et al., in preparation) but have amplitudes that

are 10 times smaller on similar angular scales. The larger-scale (∼100 arcsec) fluctuations are systematically lower on the main (approaching) jet side. The distribution of fluctuations on smaller scales is also consistent with such an asymmetry, but is not well determined. As with the transverse gradients discussed earlier, the observed position-angle rotations are too small to be sure that the RM fluctuations are due to foreground plasma, but the asymmetry between approaching and receding jets suggests an origin in a distributed magnetoionic medium surrounding the host galaxy, a possibility we now explore.

The thermal plasma associated with NGC 315 and observed using *Chandra* can be described by a beta model with a core radius of 1.55 arcsec (Worrall et al. 2003). This cannot be responsible for the RM fluctuations, which occur on far larger scales. The most likely hot plasma component to be responsible for the Faraday rotation would be associated with the poor group of galaxies surrounding NGC 315 (Nolthenius 1993; Miller et al. 2002), but has not yet been detected in X-ray observations. Since RM fluctuations are seen in both jets, a spherical distribution is plausible. In order to make a rough estimate of the parameters of the putative group component, we took a simple model for the field structure in which cells of fixed size l at radius r contain randomly orientated fields $B(r)$ (Lawler & Dennison 1982; Felten 1996). The density distribution was taken to be a beta model: $n(r) = n_0(1+r^2/r_c^2)^{-3\beta_{\rm atm}/2}$ with $B(r) \propto n(r)^N$. We derived the variation of $\sigma^2_{\rm RM}$ along the projection of the jet axis by numerical integration, assuming that the jets have $\theta = 37\overset{\circ}{.}9$ everywhere. This is a similar approach to the calculation of depolarization asymmetry by Garrington & Conway (1991) and Tribble (1992); our code also reproduces the analytical results of Felten (1996) for $\theta = 90^\circ$ and $N = 0$ or 0.5. Following Dolag et al. (2001) and Dolag (2006), we assumed that $B(r) \propto n(r)$ or $N = 1$ (an empirical result derived from RMs of radio sources in and behind cluster and rich groups). Our detection of RM variations on a range of scales is qualitatively consistent with the idea that the power spectrum of the magnetic field fluctuations is a power law (Tribble 1991; Enßlin & Vogt 2003; Murgia et al. 2004; Vogt & Enßlin 2005), but our data are too noisy and poorly sampled to constrain its functional form. Murgia et al. (2004) show that a single-scale model gives a very similar relation between the RM variance $\sigma^2_{\rm RM}$ and radius r to that derived for the more realistic case of a power-law power spectrum provided that l is interpreted as the correlation length of the magnetic field. Finally, we fitted the resulting $\sigma_{\rm RM}$ curves by eye to the profiles of RM fluctuations on different scales in Figs 13(b) and (c). We fixed the value of $\beta_{\rm atm} = 0.5$ and adjusted the core radius to give a reasonable fit to the profile. For both plots, we found that $r_c \approx 225$ arcsec gave an adequate fit. Strictly speaking, $\sigma^2_{\rm RM}$ is the RM variance evaluated over a window much larger than the maximum fluctuation scale, whereas the profiles in Fig. 13 describe fluctuations over two different ranges of scale. We have therefore added the two model variances to give a rough estimate of the total (the curves shown in Figs 13(b) and (c) actually have the same amplitude). Note that the process of removing a linear trend from the RM profile will have suppressed some power in large-scale fluctuations, particularly transverse to the jet. The amplitude of the model variance profile is related to the central density and field, and to the correlation length (Felten 1996): $(n_0/{\rm m}^{-3})^2(B_0/{\rm nT})^2(l/{\rm kpc}) \approx 700$. This is a very rough estimate, but is enough to establish that a low-density group-scale gas component with a low magnetic field can generate the observed Faraday rotation. Plausible parameters might be $n_0 \approx 600\,{\rm m}^{-3}$, $B_0 \approx 0.015$ nT (0.15 μG) and $l \approx 10$ kpc. We note that the recollimation of the jets may also require a large-scale hot-gas component.

6 MAGNETIC FIELD STRUCTURE

Vectors whose magnitudes are proportional to p at zero wavelength and whose directions are those of the apparent magnetic field inferred from the rotation-measure fit of Section 5.1 are plotted in Fig. 15. At higher resolution, we derived the apparent field direction by interpolating the RM image on to a finer grid and using it to correct the observed 5-GHz position angles (Fig. 16). The apparent field structure in the flaring region (up to ≈70 arcsec from the nucleus) is discussed extensively by Canvin et al. (2005). Here, we concentrate on larger scales, after the jets recollimate.

The signal-to-noise ratio for individual points, particularly at the jet edges, is often <3 in linear polarization, causing them to be blanked in Figs 15 and 16. In particular, it is impossible to see whether the parallel-field edge continues to large distances in the main jet. We therefore adopted the following procedure to derive the average degree of polarization.

(i) We first corrected the observed 5-GHz, 2.35-arcsec position angles for Faraday rotation using the linear model derived in Section 5.1, which is defined everywhere in the field, unlike the RM image.

(ii) We then changed the origin of position angle to be along the jet axis, so that apparent field along or orthogonal to the jet appears entirely in the Q Stokes parameter (also verifying that there is very little signal in U).

(iii) We then integrated Q and I along the jet axis from 69–113 and from 113.5–157.5 arcsec from the nucleus (the same areas used for the profiles of spectral index in Fig. 7). Lack of short spacings at 5 GHz precludes extension of this analysis to larger distances.

(iv) Finally, we divided the results to give transverse profiles of Q/I. Provided that the apparent field is either along or orthogonal to the jet axis, $p = |Q/I|$. We have chosen the sign convention so that $Q > 0$ for transverse apparent field and <0 for longitudinal field.

The resulting profiles are shown in Fig. 17. Figs 15–17 show that the apparent field configuration found in the flaring region – transverse on-axis and longitudinal at the edges – persists until at least 160 arcsec in both jets. In particular, the longitudinal-field edge of the main jet is easily detected in the profiles, even though it is not clearly visible on the images. The main difference from the corresponding profiles for the flaring region (fig. 9 of Canvin et al. 2005) is that the on-axis polarization is higher in both jets at larger distances. This is a continuation of the trend in the longitudinal profile shown by Canvin et al. (2005, their fig. 8). As in the flaring region, the on-axis (perpendicular) polarization is always higher in the counter jet, reaching levels close to the theoretical maximum of $p_0 = 0.69$ for the observed spectral index. In the main jet, $p \approx 0.4$ on-axis. Both jets are very highly polarized at their edges.

Canvin et al. (2005) modelled the three-dimensional structure of the field in the outer parts of the flaring region as a mixture of toroidal and longitudinal components of roughly equal magnitude on-axis but with the former dominant at the edge of the jet. The differences between the two jets are attributed to relativistic aberration, so the fact that they persist after the jets recollimate suggests that there is little further deceleration in this region, despite the reversal in sidedness at the edges of the jets (Section 3). A decrease in the on-axis longitudinal field component, bringing the configuration closer to a purely toroidal one, would result in a polarization distribution consistent with that observed. Some longitudinal component must remain, however, otherwise p would be close to p_0 on the axis for

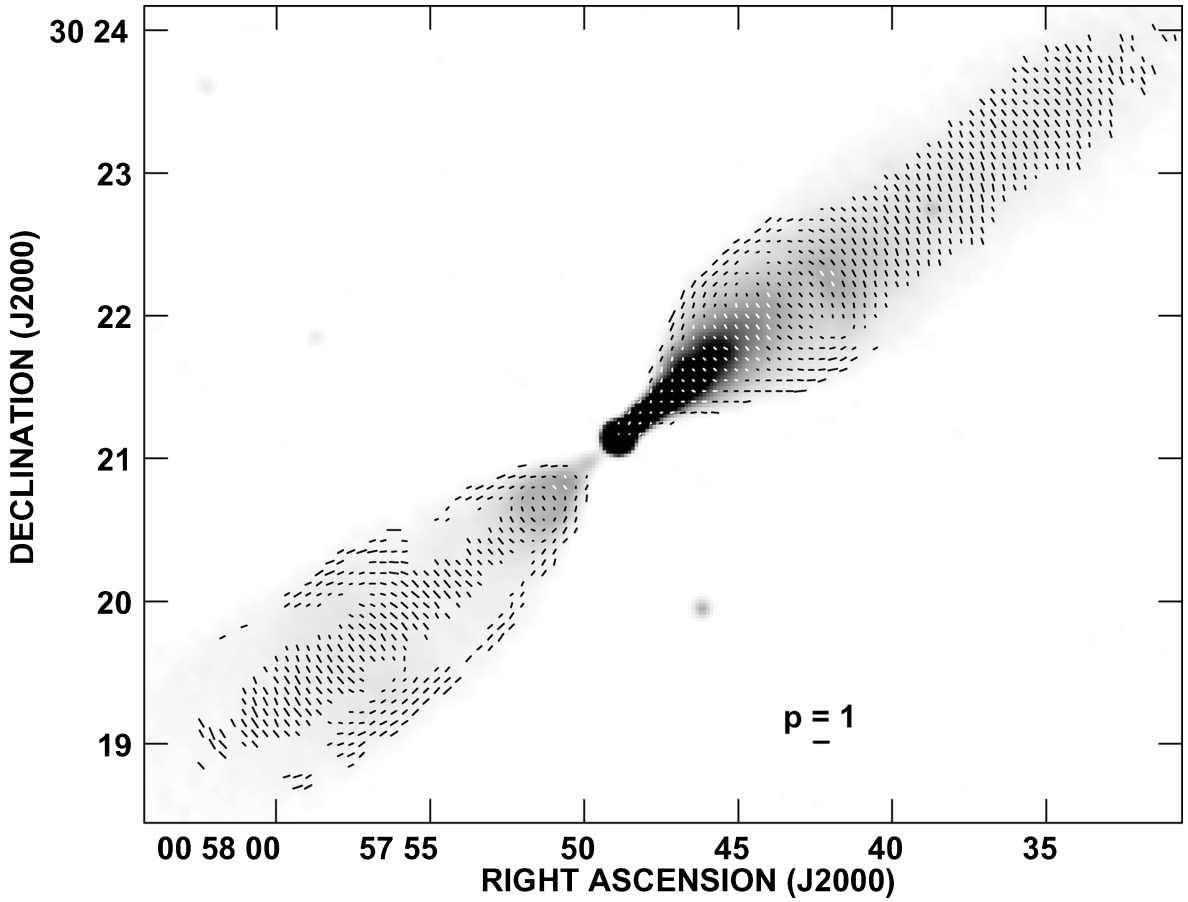

Figure 15. Vectors whose lengths are proportional to the degree of polarization at zero wavelength, $p(0)$, from the analysis of Section 5.2 and whose directions are those of the apparent magnetic field, derived from the five-frequency RM fit of Section 5.1. The vector scale is indicated by the labelled bar. The grey-scale is of total intensity at 4.985 GHz and the resolution is 5.5 arcsec FWHM.

both jets. The very high degree of polarization at the jet edge requires the radial field component to be very small, as inferred for the flaring region by Canvin et al. (2005).

7 SUMMARY

We have imaged the jets in the nearby FRI radio galaxy NGC 315 with the VLA at five frequencies in the range 1.365–5 GHz and at resolutions ranging from 45 to 1.5 arcsec FWHM. Our total intensity observations reveal new details of the structure, particularly around the sharp bend in the main jet.

The flaring regions of both jets, where they initially expand rapidly and then recollimate, show a complex and previously unknown spectral structure. Within 15 arcsec of the nucleus, the spectral index has a uniform value of $\alpha = 0.61$ in both jets. This region is associated with strong X-ray emission in the main jet, high radio emissivity, complex filamentary structure and fast flow with $\beta \approx 0.9$ (Worrall et al. 2003; Canvin et al. 2005). Between 15 and 70 arcsec, the spectrum is steeper on-axis than at the edges of the jet. We have developed a novel deprojection technique which allows us to isolate two spectral components. The first (on-axis) component forms a continuation of the jet base, its spectral index flattening gradually from 0.61 to 0.55. The second component (at the edge of the jet) has $\alpha \approx 0.44$ and is associated with a region where strong shear is inferred (Canvin et al. 2005). We speculate that two different acceleration mechanisms are involved, one associated with fast flow, dominant close to the nucleus and capable of accelerating electrons to the very high energies required to produce X-ray emission ($\gamma \sim 10^8$), the other being driven by shear and generating the flatter spectral indices seen at the edges of the jet. Both mechanisms must efficiently generate the electrons with $\gamma \sim 10^4$ which radiate at cm wavelengths. At distances $\gtrsim$70 arcsec, the spectral index is consistent with $\alpha \approx 0.47$ everywhere.

We have imaged the variations of Faraday rotation over the jets. All of the rotation is resolved and must originate mostly in foreground material. There is no detectable depolarization. The largest contributions – a constant term and a linear gradient – are probably Galactic in origin. We have also detected residual fluctuations of $\approx$1–2 rad m^{-2} rms on scales $\sim$5–100 arcsec. The amplitude of fluctuations on scales $\gtrsim$30 arcsec is larger by a factor of $\approx$2 for the counter jet, consistent with an origin in magnetoionic material around the source, but not in the known X-ray-emitting halo, whose core radius is too small. We model the Faraday-rotating medium as a spherical halo with a core radius $\approx$225 arcsec and derive an approximate value for the product $(n_0/\mathrm{m}^{-3})^2\,(B_0/\mathrm{nT})^2\,(l/\mathrm{kpc}) \approx 700$, where n_0 is the central density, B_0 the central magnetic field and l is the magnetic field correlation length. Our analysis is therefore consistent with models of Faraday rotation proposed for rich clusters (e.g. Carilli & Taylor 2002), but requires much lower densities and field strengths. We predict that a tenuous, group-scale halo should be detectable in sensitive X-ray observations; measurement of its density will allow us to estimate the magnetic field strength.

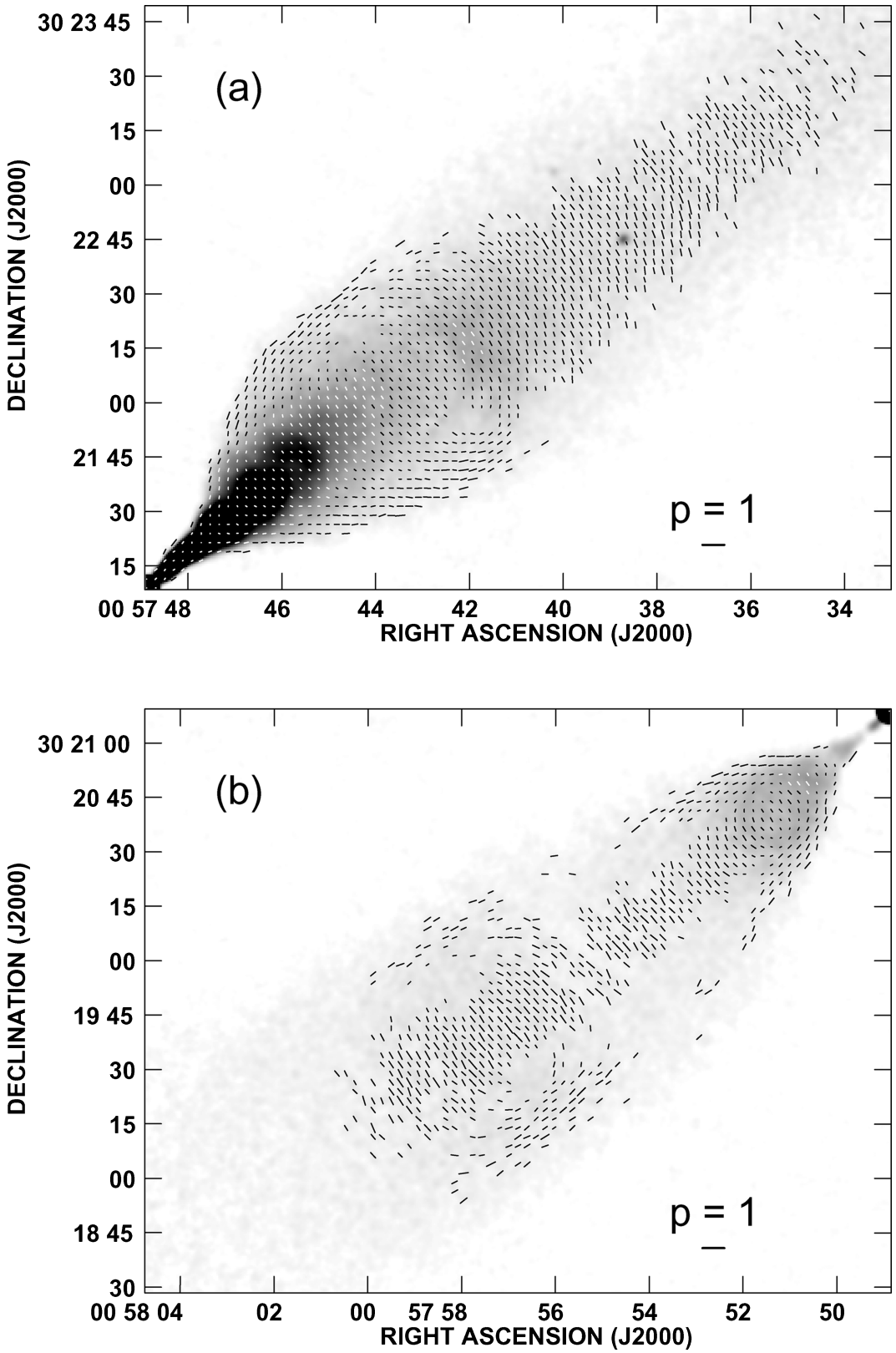

Figure 16. Vectors whose lengths are proportional to the degree of polarization p at 4.985 GHz and whose directions are those of the apparent magnetic field, derived by rotating the observed $\boldsymbol{E}$-vector position angles at that frequency by amounts derived from the five-frequency RM fit of Section 5.1 interpolated on to a finer grid. The vector scale is indicated by the labelled bars. The grey-scale is of total intensity at 4.985 GHz and the resolution is 2.35 arcsec FWHM. (a) Main jet; (b) counter jet.

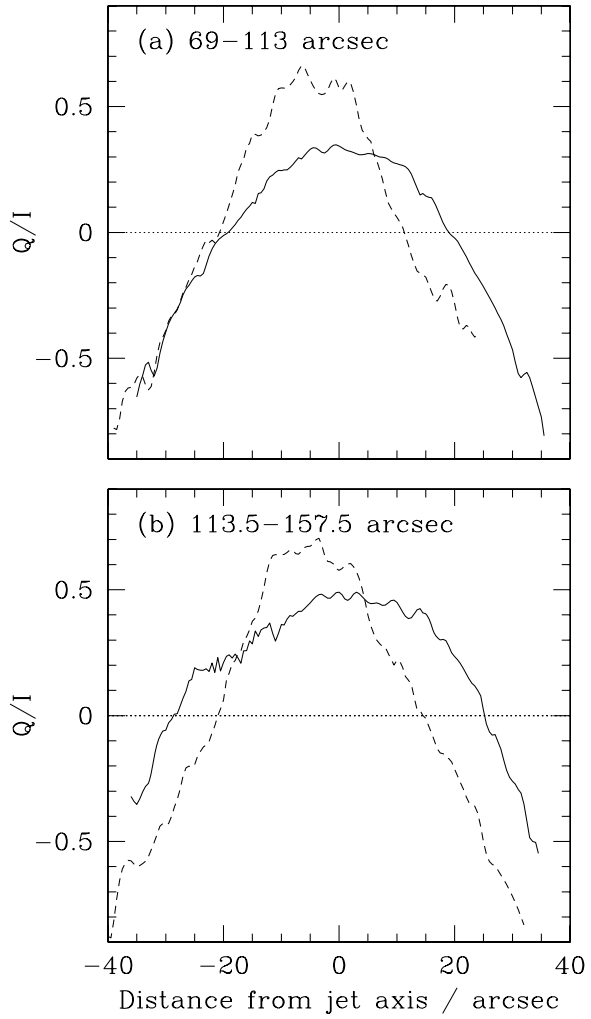

Figure 17. Profiles of Q/I for the main and counter jets, integrated along the jet axis as described in the text. $|Q/I| = p$ for an apparent field direction either along or orthogonal to the jet, as seen here. $Q/I > 0$ corresponds to a transverse apparent field, $Q/I < 0$ to a longitudinal one. Full line: main jet; dashed line: counter jet. (a) 69–113 arcsec; (b) 113.5–157.5 arcsec (the areas are the same as in Fig. 7).

We have derived the apparent magnetic field direction (corrected for Faraday rotation) and degree of polarization at distances between 70 and 160 arcsec from the nucleus. The structure is qualitatively similar to that seen in the flaring region, with transverse field on-axis and longitudinal field at the edges of both jets, but the degree of polarization on-axis is larger. The difference in polarization structure between the main and counter jets observed in the flaring region by Canvin et al. (2005) persists at larger distances. This can be explained fully as an effect of differential aberration on radiation from intrinsically identical jets, as long as their velocities remain significantly relativistic on the relevant scales. The asymmetry in RM fluctuation amplitude is consistent with the jet orientation required by this analysis and the presence of a tenuous, magnetized group halo.

The large angular size of the flaring region in NGC 315 and our use of deep observations at several frequencies has allowed us to image spectral variations at a level of detail not yet achieved in any other jet. Taken together with X-ray imaging and modelling of the jet velocity field, this has given important insights into the particle acceleration mechanisms. It will be interesting to see whether our results apply to other FRI jets and to study the spectral variations in NGC 315 over a wider frequency range.

ACKNOWLEDGMENTS

JRC acknowledges a research studentship from the UK Particle Physics and Astronomy Research Council. The National Radio Astronomy Observatory is a facility of the National Science Foundation operated under cooperative agreement by Associated Universities, Inc. We thank Greg Taylor for the use of his rotation-measure code, Karl-Heinz Mack for providing the 327-MHz WSRT image, Frank Rieger for discussions on shear acceleration and the referee for helpful comments. We also acknowledge the use of the HEALPIX package (http://healpix.jpl.nasa.gov) and the provision of the models of Dineen & Coles (2005) in HEALPIX format.

REFERENCES

Barth A. J., Filippenko A. V., Moran E. C., 1999, ApJ, 525, 673
Blandford R. D., 1993, in Burgarella, D., Livio, M., O'Dea, C. P., eds, STScI Symp. Ser. Vol. 6, Astrophysical Jets. Cambridge Univ. Press, Cambridge, p. 15
Bridle A. H., 1982, in Heeschen, D. S., Wade, C. M., eds, IAU Symp. Vol. 97, Extragalactic Radio Sources. Reidel, Dordrecht, p. 121
Bridle A. H., Davis M. M., Meloy D. A., Fomalont E. B., Strom R. G., Willis A. G., 1976, Nat, 262, 179
Bridle A. H., Davis M. M., Fomalont E. B., Willis A. G., Strom R. G., 1979, ApJ, 228, L9
Bridle A. H., Chan K. L., Henriksen R. N., 1981, J.R. Astron. Soc. Can., 75, 69
Burn B. J., 1966, MNRAS, 133, 67
Canvin J. R., Laing R. A., 2004, MNRAS, 350, 1342
Canvin J. R., Laing R. A., Bridle A. H., Cotton W. D., 2005, MNRAS, 363, 1223
Carilli C. L., Taylor G. B., 2002, ARA&A, 40, 319
Cotton W. D., Feretti L., Giovannini G., Lara L., Venturi T., 1999, ApJ, 519, 108
Dineen P., Coles P., 2005, MNRAS, 362, 403
Dolag K., 2006, Astron. Nachr., in press
Dolag K., Schindler S., Govoni F., Feretti L., 2001, A&A, 378, 777
Enßlin T. A., Vogt C., 2003, A&A, 401, 835
Enßlin T. A., Simon P., Biermann P. L., Klein U., Kohle S., Kronberg P. P., Mack K.-H., 2001, ApJ, 549, L39
Fanaroff B. L., Riley J. M., 1974, MNRAS, 167, 31P
Felten J. E., 1996, in Trimble V., Reisenegger A., eds, ASP Conf. Ser. Vol. 88, Clusters, Lensing and the Future of the Universe. Astron. Soc. Pac., San Francisco, p. 271
Fomalont E. B., Bridle A. H., Willis A. G., Perley R. A., 1980, ApJ, 237, 418
Garrington S. T., Conway R. G., 1991, MNRAS, 250, 198
Hardcastle M. J., Birkinshaw M., Worrall D. M., 2001, MNRAS, 326, 1499
Hardcastle M. J., Worrall D. M., Birkinshaw M., Laing R. A., Bridle A. H., 2002, MNRAS, 334, 182
Hardcastle M. J., Worrall D. M., Birkinshaw M., Laing R. A., Bridle A. H., 2005, MNRAS, 358, 843
Ho L. C., Filippenko A. V., Sargent W. L. W., Peng C. Y., 1997, ApJS, 112, 391
Huchra J. P., Geller M. J., de Lapparent V., Corwin H. G. Jr 1990, ApJS, 72, 433
Jägers W. J., 1987, A&AS, 71, 75
Katz-Stone D. M., Rudnick L., 1997, ApJ, 488, 146
Katz-Stone D. M., Rudnick L., Butenhoff C., O'Donoghue A. A., 1999, ApJ, 516, 716
Killeen N. E. B., Bicknell G. V., Ekers R. D., 1986, ApJ, 302, 306
Laing R. A., 1981, ApJ, 248, 87

Laing R. A., Bridle A. H., 2002a, MNRAS, 336, 328
Laing R. A., Bridle A. H., 2002b, MNRAS, 336, 1161
Laing R. A., Bridle A. H., 2004, MNRAS, 348, 1459
Lawler J. M., Dennison B., 1982, ApJ, 252, 81
Lazio T. J. W., Waltman E. B., Ghigo F. D., Fiedler R. L., Foster R. S., Johnston K. J., 2001, ApJS, 136, 265
Leon S., Lim J., Combes F., Dihn-V-Trung, 2003, in Collin S., Combes F., Shlosman I., eds, ASP Conf. Ser. Vol. 290, Active Galactic Nuclei: From Central Engine to Host Galaxy. Astron. Soc. Pac., San Francisco, p. 525
Linfield R., 1981, ApJ, 244, 436
Longair M. S., 1994, High Energy Astrophysics. Cambridge Univ. Press, Cambridge
Mack K.-H., Klein U., O'Dea C. P., Willis A. G., 1997, A&AS, 123, 423
Mack K.-H., Klein U., O'Dea C. P., Willis A. G., Saripalli L., 1998, A&A, 329, 431
Miller N. A., Ledlow M. J., Owen F. N., Hill J. M., 2002, AJ, 123, 3018
Murgia M., Govoni F., Feretti L., Giovannini G., Dallacasa D., Fanti R., Taylor G. B., Dolag K., 2004, A&A, 424, 429
Noel-Storr J., Baum S. A., Verdoes Kleijn G., van der Marel R. P., O'Dea C. P., de Zeeuw P. T., Carollo C. M., 2003, ApJS, 148, 419
Nolthenius R., 1993, ApJS, 85, 1
Parma P., de Ruiter H. R., Capetti A., Fanti R., Morganti R., Bondi M., Laing R. A., Canvin J. R., 2003, A&A, 397, 127
Perlman E. S., Wilson A. S., 2005, ApJ, 627, 140
Rieger F. M., Duffy P., 2004, ApJ, 617, 155
Rieger F. M., Duffy P., 2005, in Chen P., Bloom E., Madejski G., eds, 22nd Texas Symposium on Relativistic Astrophysics at Stanford. SLAC, Stanford, http://www.slac.stanford.edu/econf/C041213/
Simard-Normandin M., Kronberg P. P., 1980, ApJ, 242, 74
Simonetti J. H., Cordes J. M., 1986, ApJ, 303, 659
Taylor G. B., Ulvestad J. S., Perley R. A., 2004, The Very Large Array Observational Status Summary, NRAO, Socorro, URL: http://www.vla.nrao.edu/astro/guides/vlas/current/
Trager S. C., Faber S. M., Worthey G., Gonzalez J. J., 2000, AJ, 119, 1645
Tribble P. C., 1991, MNRAS, 250, 726
Tribble P. C., 1992, MNRAS, 256, 281
van Gorkom J. H., Knapp G. R., Ekers R. D., Ekers D. D., Laing R. A., Polk K. S., 1989, AJ, 97, 708
Venturi T., Giovannini G., Feretti L., Comoretto G., Wehrle A. E., 1993, ApJ, 408, 81
Verdoes Kleijn G. A., Baum S. A., de Zeeuw P. T., O'Dea C. P., 1999, AJ, 118, 2592
Vogt C., Enßlin T. A., 2005, A&A, 434, 67
Wardle J. F. C., Kronberg P. P., 1974, ApJ, 194, 249
Willis A. G., Strom R. G., Bridle A. H., Fomalont E. B., 1981, A&A, 95, 250
Worrall D. M., Birkinshaw M., 2000, ApJ, 530, 719
Worrall D. M., Birkinshaw M., Hardcastle M. J., 2003, MNRAS, 343, L73
Xu C., Baum S. A., O'Dea C. P., Wrobel J. M., Condon J. J., 2000, AJ, 120, 2950
Young A., Rudnick L., Katz D., Delaney T., Kassim N. E., Makishima K., 2005, ApJ, 626, 748

This paper has been typeset from a TEX/LATEX file prepared by the author.